Spectrochimica Acta Part B: Atomic Spectroscopy 237 (2026) 107454

Contents lists available at ScienceDirect

Spectrochimica Acta Part B: Atomic Spectroscopy

journal homepage: www.elsevier.com/locate/sab

Transferable calibration coefficients for semi-quantitative analysis by Laser Induced Breakdown Spectroscopy (LIBS) in samples containing calcium

V. Lazic [a,*], M. Markovic [b], B.D. Stankov [c], F. Andreoli [d], C. Ulrich [e], M. Kuzmanovic [b]

[a] ENEA, Lab. NUC-TECFIS-DIM, Via E. Fermi 45, 00044 Frascati, RM, Italy
[b] Faculty of Physical Chemistry, University of Belgrade, Belgrade 11158, Serbia
[c] Institute of Physics, University of Belgrade, Belgrade 11080, Serbia
[d] ENEA, Lab. NUC-FUSEN-TEN, Via E. Fermi 45, 00044 Frascati, RM, Italy
[e] Fraunhofer Institute for Chemical Technology ICT, Energetic Materials Department, Joseph-von-Fraunhofer-Str. 7, 76327 Pfinztal, Germany

ARTICLE INFO

Keywords:
LIBS
Laser spectroscopy
Calibration
Quantitative
Soils
Powders
Matrix effect

ABSTRACT

This work establishes a framework for testing and developing calibration coefficients for multi-elemental analysis by LIBS, that are transferrable to various instruments under specific experimental conditions: measurements in air, full optical collection of the plasma plume, apparent plasma temperature and electron density within 6500–7500 K and 1–2 × 10^{17} cm^{-3}, respectively. Here, the plasma was produced by ns laser pulses at 1064 nm, with energy of 30 mJ while for its detection we used high resolution compact spectrometers. Calibration coefficients for 14 elements were derived respect to one Ca I line (443.50 nm) considering that Ca is a common element in natural samples. The calibration coefficients were obtained from: (i) extrapolated linear peak growths, produced by changing the sample mass on a solid support (Si wafer or Al); (ii) peaks normalized on the Ca line. Their validity interval is specified while the inherent variations with the element abundance and plasma parameters are explained. The initial calibration involved nine different samples, including a multi-element standard, rock, soils ash, coal, and carbonate's mixture, while the validation was applied on two soil samples, both in form of particles on wafer and pressed into pellets. Calibration coefficients based on the linear slope produced quantification of 13 elements within accuracy of ±30% while the use of the line ratios increased the error for some considered elements. To facilitate transfer of the coefficients to other experiments, we provide practical instructions and limits of applicability. The transition from relative to absolute element concentration measurements is also explained in the text.

1. Introduction

Laser-induced breakdown spectroscopy (LIBS) is a technique for elemental analysis that exhibits a range of unique advantages compared to competing analytical methods [1,2]. Besides its speed and the capability for in-situ, on-line, and remote measurements, LIBS can also provide fine surface [3] and in-depth mapping [4] of the chemical sample composition. Unlike techniques based on X-ray spectra, LIBS has no limitations when analysing light elements. Direct sample probing or with minimal sample preparation represents an important advantage over standard laboratory methods, such as inductively coupled plasma atomic emission spectroscopy (ICP-AES) and inductively coupled plasma mass spectrometry (ICP-MS), that require laborious and destructive sample preparation, comprising a dilution and digestion.

LIBS technique is widely used for qualitative analysis of various samples while a high accuracy of the element quantification, similarly to other analytical methods, usually requires the initial univariate or multivariate calibration using matrix-matched samples. The matrix effect regards chemical and physical sample properties, including state of the analysed surface, and it is particularly pronounced in LIBS due laser-sample interaction. Changes in the sample matrix might lead to differences in the ablation rate, plasma shape and dimensions, plasma temperature and electron density, and chemical reactions during the signal acquisition window. Various calibration strategies in LIBS have been recently reviewed [5] and one of the most common regards creations of Curve of Growths (COGs) for each analytical line, where the linearity exists inside a limited concentration range and the signal is dependent on the acquisition parameters and collection geometry [6,7]. If the laser

---

[*] Corresponding author.
E-mail address: violeta.lazic@enea.it (V. Lazic).

https://doi.org/10.1016/j.sab.2026.107454
Received 30 October 2025; Received in revised form 12 January 2026; Accepted 12 January 2026

produced plasma has parameters different from one sample to another, the calibration graphs remain poor unless the signal is corrected for the plasma temperature at least [8,9]. A complete correction procedure for calibration in presence of different plasma parameters from one sample to another is described in [10], and this approach also allows transferring the calibration curves from reference materials to real samples. The time-consuming calculations of plasma parameters, accompanied by not negligible errors, might be replaced by empirical correction through ratio of ionic to atomic line pairs [11]. In any case, accuracy and precision in the element quantification can be improved by applying some signal normalization, including the use of internal standards and other reference signals, as well as multivariate correction [12].

Another approach for determining element concentrations in samples is so called calibration-free (CF) method that assumes that the plasma is uniform, optically thin and in Local Thermal Equilibrium (LTE), that all elements in sample are detected and that their sum equal to 100% [13]. This method requires the signal acquisition over a wide spectral range where the spectral sensitivity of the instrument must be carefully calibrated, then calculations of the plasma temperature and electron density, and use of the analytical lines with known transition constants. There are various critical issues related to the CF method [14,15], but it might produce satisfactory results for major constituents in some sample types, while the closure to 100% becomes critical in presence of elements difficult to detect by LIBS. On uniform bulk materials, like optical glasses, where it is feasible to perform a large number of measurements, the CF approach combined with the measurements of line's absorption coefficients and plasma modelling, can lead to semi-quantitative results also for some trace elements [16].

An accurate multi-elemental quantitative LIBS analysis is very difficult to achieve on complex materials, such as geological samples where the matrix effect is particularly pronounced [17–20]. Through calibration over 69 rock samples and application of partial least squares regression (PLSR), semi-quantitative results by ChemCam instrument were obtained for abundances of Si, Ti, Al, Fe, Mn, Mg, Ca, and K; the accuracy error was below 30% and 25% for Si and Fe, respectively, while much better results were obtained on the other considered elements [19]. Determining of a relative concentration of Al, Ca, Fe, K, Na, Si, and Ti respect to Mg content, after calibration involving 22 powdered rocks, produced relative prediction errors between 9.5% and 33% [21]. LIBS applied for measuring of micronutrient elements B, Cu, Fe, Mn, and Zn in plant materials, showed the errors in concentration measurement up to 55% for univariate calibration and 113% for PLSR approach [22]. By using a hand-held LIBS instrument and calibration on 137 soil samples pressed into pellets, through multivariate calibration the best coefficients of determination were of 0.86, 0.75, 0.77, and 0.81 for Ca, Mg, K, Fe and Al, respectively; other nutrients, such as Mn and P, could only be determined qualitatively [23]. A comparison of PLSR and support vector regression (SVR), applied on soil samples, showed the determination errors within 10% for Si, Al and Sr, between 10% and 20% for Mg, Ca, Na, K, Mn, Ba, Ti, and Cr, and 45% for Cu [24].

The use of PLS, machine learning (ML) or artificial neural networks (ANN) can mitigate but not resolve the problems related to the matrix effect for all elements to be measured. For example, determination of trace Ag in soils reached the accuracy of 5–6% [25], but the maximum achieved predictive ability for K in soils was of 0.84 only [26]. Even if the training dataset is large and includes different reference soils and rocks, a high prediction accuracy for all elements measured simultaneously has not been achieved by LIBS [27]. Recently, the spectra acquired with different laser energies, corresponding to different plasma temperatures, were also included in the training sets [28,29].

The initial multi-element calibration for LIBS requires a huge effort and use of numerous reference materials, so it is of great interest to achieve a calibration method that could be transferred from one instrument to another. Lepore et al. [29] made a step towards by defining the data collection and transfer protocols, and by applying spectral line binning to share the calibration spectra among three different LIBS instruments. Here, the calibration transfer was performed using the Piecewise Direct Standardization with Partial Least Squares (PDS-PLS) calibration transfer algorithm in PyHAT, that is an open-source Python [30]. Through tests for the prediction accuracy regarding oxides from seven elements (Si, Ti, Al, Fe, Mg, Ca, Na and K), it was found that minor differences in instrument resolution do not prohibit mixing training and test spectra from two different sources. The best prediction accuracies were achieved by down-sampling high-resolution spectra to a low-resolution through binning peak areas, and matching of the plasma parameters was decisive to effectively transfer training spectra to test conditions.

In this work we explore a possibility to establish calibration coefficients for 14 elements with respect to Calcium, in a certain range of the element concentrations and plasma parameters, with the scope to move towards the calibration transfer among different high to moderate resolution LIBS instruments. We selected Calcium as internal standard, since this element commonly appears in samples of geological and biological origins, and it is easy to detect by LIBS. In this approach, the supplied calibration coefficients could be used to estimate the element abundancies in a way analogue to the calibration-free method, considering that the summed concentrations of all detected elements or their specific forms (e.g. oxides) is 100%. Alternatively, knowledge of the abundance of Ca in samples leads to the concentrations of other elements within the determination errors. Instead of complex mathematical approaches or data training models that burden any meaning of real physical/chemical processes, without solving the analytical problems in LIBS, we opted to consider simply various peak intensities from elements in samples. Here derived calibration coefficients regard both the line peak ratios and the relative peak growths [31], which behaviours we support by theoretical simulations. The intensity ratios of some spectral lines were simulated to assess the impact of plasma temperature and electron density, whose variations affect both the initial calibration and the successive estimation of the relative element concentrations. In the present experiment, we minimized the matrix effect through LIBS sampling of particles on Silica wafer [31,32] or Aluminium substrate. This experimental approach is very simple, it requires only a small sample amount (< 1 mg), and allows generating spectra with quite different peak intensities and with variable plasma parameters, dependently on sample mass inside the laser spot. Validation of the results was extended from particles on wafer to pressed soil pellets, where we also evaluated the effect of departure from the plasma parameters, found in the calibration phase, on the analytical results.

2. Experimental

2.1. Samples

The sample set used for calibration consisted in materials with known elements masses or concentrations: a 21 elements standard (ST21), one milled rock material, four soils, one ash and one coal sample, plus a mixture 50:50 of $CaCO_3$ and $BaCO_3$ powders prepared in laboratory. The powdered samples were evenly distributed on a substrate, and 10–25 single shot LIBS spectra were collected to cover a wide range of spectral intensities, dependent on sample mass and its distribution inside the laser spot. During the measurements, it was necessary to add particles more times because of the surface cleaning effect by laser induced shockwaves. In most cases, Si wafer was used as substrate (thickness 0.55 mm, SiO_2 layer 285 nm) because of its high purity and enhancement of the plasma emission [31,32]. In one case, a clean aluminium substrate was used to also evaluate Si/Ca line ratios.

The original reference material ST21 is a water solution containing 100 mg/L each of following elements: As, Be, Ca, Cd, Co, Cr, Cu, Fe, Li, Mg, Mn, Mo, Ni, Pb, Sb, Se, Sr, Ti, Tl, V, Zn, in HNO_3 2%/tr. HF, tartaric acid. The standard was further diluted in milli-Q water to prepare solutions with concentrations of 1 mg/L, 10 mg/L and 100 mg/L of each element. These solutions were deposited on wafer as spots, by a drop-ondemand printer (Nanoplotter NP 2.1 from GeSIM); the single droplets had a controlled volume between 300 pL and 350 pL [33]. At a single spot, 3 to 32 droplets have been deposited to result in the different solid deposits after evaporation of the solvent. The masses left on the wafer surface were 5, 10, 50, 100, 250 or 500 pg for each element. For each elements mass, the spots were deposited in a grid 3 × 3 with 3 mm spacing. The diameter of the largest printed spot, corresponding to 500 pg load per element, was of about 0.1 mm, thus smaller than the laser spot diameter (0.3 mm).

Validation of the calibration coefficients was performed on: Soil#2 particles on wafer (the combination not included in the calibration), and on two soils pressed into pellets. The pellets were probed at 10 points distanced for at least 2 mm each other and so obtained single shot spectra were successively averaged. The measurements on pellets were performed a year later than those on spots/particles over a substrate, aimed to also evaluate a robustness of the method considering that, meanwhile, the LIBS instrument was used in three outdoor campaigns and re-aligned various times. The details about the samples used for calibration and validation are reported in Table 1.

2.2. LIBS apparatus

The LIBS instrument used here, was initially developed for examination of trace materials on a crime scene, and its full description and performances are reported in previous work [33]. In the present experiment, we used the instrument in a static mode, where a substrate/pellet was placed on a holder with micrometric X-Y-Z slits. The LIBS signal was generated by a diode pumped Nd:YAG laser (BrightAerospace, model BAS_CDL-1064-50 mJ-DB) emitting pulses of 6.5 ns duration at 1064 nm. The laser energy delivered on sample was set to 30 mJ and the laser spot diameter was of about 0.3 mm. The laser was operated manually to acquire the spectra after shifting the sample and/or adding new particles on the substrate.

The signal collection is based on two identical optical systems, each containing a pair of parabolic mirrors with UV enhanced Al coating, and one 2 m long bundle of four quartz fibres with core diameter of 600 μm. Three of these fibres bring the signal to the spectrometers while the fourth fibre is used to transmit the pointing light (at 635 nm) to the target and so facilitate its correct positioning. The plasma emission is detected by six compact spectrometers (Avantes, model AvaMINI 2048), customized to cover the interval from 180 nm to 875 nm, with spectral resolution reported in Table 2 together with the used range. The spectral resolution, expressed as full width half maximum (FWHM), has been revised - now it is based on the minimum Gaussian width of some detected not resonant LIBS peaks instead of previously retrieved (higher) values by using a low-pressure calibration HgAr lamp [33].

The spectrometer detectors have a minimum integration time of 30 μs, adopted in the present experiment, and they are externally pre-triggered and synchronized to achieve the effective detection delay starting from the laser pulse. Basing on the previous signal optimization for particles on wafer [33], the acquisition delay was set to 2000 ns. In case of measurements on pressed pellets, the comparative acquisitions were done also for delays of 1700 and 1200 ns. The image of sample was automatically acquired before arrival of the laser pulse while the additional photos by the instrument after the LIBS signal acquisition were taken as well.

For here performed calibrations, aimed to be transferred to other instruments, it is of fundamental importance that the whole plasma emission is collected. In the present set-up, the back projected spot size of the collecting fibres had oval shape on sample with the axis lengths of about 1.5 mm and 2.0 mm, which are significantly larger than the laser spot size (diameter 0.3 mm). The relative Spectral Response (S_R) of the detection system that comprises the fibre bundles and spectrometers, was determined by a radiatively calibrated Deuterium-Halogen lamp (DH-2000, Ocean Optics), used with the cosine-corrected irradiance probe (CC-3). Here, the exclusion of the two metallic mirrors that direct the signal towards a fibre bundle, means that below 250 nm, where the used mirrors start to lose their reflectivity, the effective spectral response of the whole system is slightly lower than that reported in the following section.

Table 1
Sample set for calibration and validation.

Sample	Details	Form	Elements considered or detected	Notes
Calibration				
ST21#W	Water solution 21 elements with same %wt	nano-plotted on wafer and dried, 5, 10, 50, 100, 250, 500 pg*	Ca, Cr, Cu, Fe, Li, Mg, Mn, Pb, Sr, Ti, V, Zn	Impurities: C, K, Na, Al; spectra averaged over six 6 points.
Rock#W	NCS DC73302	Particles on wafer	Al, Ba, Ca, Cr, Cu, Fe, K, Li, Mg, Mn, Na, Sr, Ti, V, Zn	14 single shot spectra
Soil1#W	NIST2709a - San Joaquin Soil (agricultural)	Particles on wafer	Al, Ba, Ca, Cr, Cu, Fe, K, Mg, Mn, Na, Sr, Ti, V	14 single shot spectra
Soil2#A	NIST2710a - Montana soil with high trace element concentrations	Particles on Al plate	Ba, Ca, Cr, Cu, Fe, K, Mn, Na, Pb, Si, Sr, Ti, V, Zn	10 single shot spectra
Soil3#W	NIST2711a - Montana soil with moderate trace element concentrations	Particles on wafer	Al, Ba, Ca, Cr, Cu, Fe, K, Mg, Mn, Na, Pb, Sr, Ti, Zn	14 single shot spectra
Soil4#W	Sandy Clay Soil ISE 992	Particles on wafer	Al, Ba, Ca, Cr, Cu, Fe, K, Li, Mg, Mn, Na, Sr, Ti, V, Zn	15 single shot spectra
ASH#W	Coal fly ash 1633a	Particles on wafer	Al, Ca, K, Mg, Mn, Na, Sr, V, Zn	15 single shot spectra
COAL#W	Bituminous coal 1632b	Particles on wafer	Al, Ba, Ca, Cr, Cu, Fe, K, Li, Mg, Mn, Na, Ti	25 single shot spectra
CaBa#W	50:50 mixture of $CaCO_3$ and $BaCO_3$	Particles on wafer	Ba, Ca	14 single shot spectra
Validation				
Soil2#W	Soil NIST2710a	Particles on wafer	Ba, Ca, Cr, Cu, Fe, K, Mg, Mn, Na, Pb, Sr, Ti, V, Zn	18 single shot spectra
Soil2#P	Soil NIST2710a	Pressed pellets	Ba, Ca, Cr, Cu, Fe, K, Mg, Mn, Na, Pb, Sr, Si, Ti, Zn	Spectra averaged over 10 points
Soil3#P	Soil NIST2711a	Pressed pellets	Al, Ba, Ca, Cr, Cu, Fe, K, Mg, Mn, Na, Pb, Si, Sr, Ti, Zn	Spectra averaged over 10 points

* Mass per element.

3. Results and discussion

3.1. LIBS signal dependency on the ablated element mass and on plasma parameters

The LIBS signal intensity from particles placed on wafer strongly depends on sample mass and its distribution within the laser spot (Fig. 1). Although the sample mass inside the laser spot is estimated to

Table 2
Characteristics of the spectrometers: grating, available and used wavelength range, and spectral resolution measured at the specified wavelengths.

No.	Grating (gr/mm)	Effective range (nm)	Used range (nm)	Resolution (nm)
1	3600	178–259	180–250	0.053 (193.1 nm) - 0.045 (238.9 nm)
2	3600	248–318	250–311	0.0046 (257.8 nm) – 0.042 (293.3 nm)
3	2400	307–423	311–418	0.074 (339.4 nm) – 0.056 (404.6 nm)
4	1800	407–561	418–555	0.10 (440.8 nm) – 0.087 (553.5)
5	1800	546–670	555–668	0.11 (585.7 nm) – 0.088 (646.2 nm)
6	1200	646–875	668–875	0.16 (714.8 nm) – 0.18 (854.2)

<1 ng, very intense spectral lines from sample were obtained. In the first reported case (Fig. 1a) for Rock# particles, the Ca II doublet near 395 nm even reached the detector's saturation. Intense Mn, Fe and Sr peaks were also observed, where their certified concentrations are of 604 ppm, 5.29% and 790 ppm, respectively. By reducing the particle mass inside the laser spot, the spectra become dominated by Si lines from the wafer, especially in the UV region (Fig. 1b). However, the peaks from Sr II and Fe I remain intense while Mn I triplet close to 403 nm is still above the detection threshold. In our previous experiments, it was found that excessive coverage of the Si wafer by particles or trace liquids, significantly reduces the LIBS signal from sample because this substrate enhances the plasma formation [31,32].

To systematically assess the effect of the sample mass on the LIBS signal, six replicated measurements were performed on nano-plotted ST21 containing element masses between 5 pg and 500 pg. The spectra were successively averaged to increase Signal-to-Noise Ratio (SNR), particularly for weak peaks at low element masses. Comparative sampling at clean wafer substrate was also performed. Selected analytical lines are listed in Table 3 where for some elements we considered different transitions; the H_α line was used to estimate the plasma electron density. Relative Spectral Response (S_R) reported in the table was normalized to value of 1000.

Most of the detected analytical lines show the Gaussian profile while intense resonant peaks, as well as the Si I and H_α lines, required fitting by the Voigt's function where the Gaussian width was extrapolated from Table 2. In this work, we opted for calibration through the calculated peak heights because: (i) for the given plasma parameters, element concentrations and spectrometer resolutions, the line broadening was absent for most of the analytical lines; (ii) for not well isolated lines or weak peaks, the fitted line integral might produce large errors while the peak values could be also approximated by the maximum intensity after the baseline subtraction. In following, the peak intensities are always referred to the fitted peak heights.

Initially, the line intensities from sample ST21 on wafer rapidly increase with the element mass, but later this growth is slowed down or even inverted, particularly in case of intense resonant lines, such as Ca I at 422.67 nm and Mg I at 285.21 nm (Fig. 2a). Simultaneously, the emission from Si I (288.16 nm) decays above the element mass of 50 pg due to substrate screening by the deposited sample material (Fig. 2b).

The electron density N_e was retrieved from H_α line fitted by the Voigt's function and assuming that the Stark broadening w_S depends on the Lorentzian w_L and the Gaussian w_G linewidth as [34]:

$$w_S = 0.5346 \bullet w_L + \sqrt{0.2169 \bullet w_L^2 + w_G^2} \tag{1}$$

Since the contribution of the Doppler profile is negligible compared to the instrumental broadening, here of 0.088 nm, the latter value was adopted as w_G in eq.1. Electron number density was then calculated by the following formula [35]:

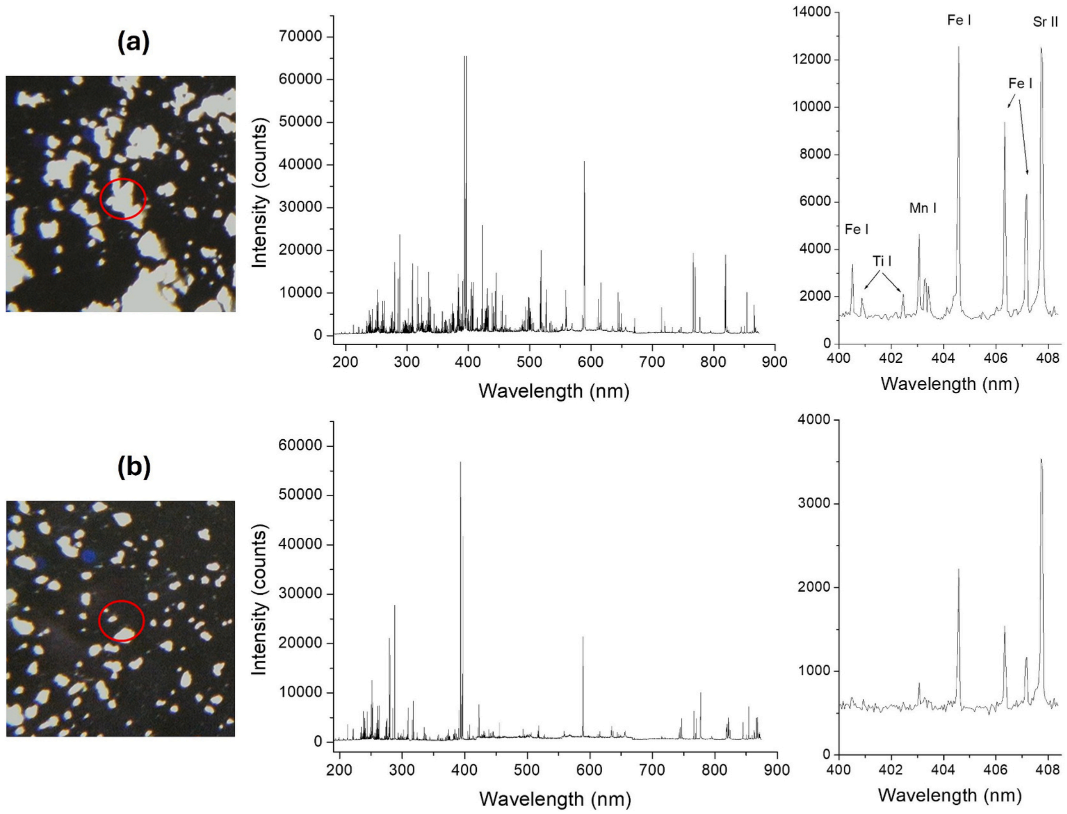

Fig. 1. Two examples of Rock#W particle distributions inside the laser spot (red circle) and the corresponding single shot spectra in full scale and in a selected detail. (For interpretation of the references to colour in this figure legend, the reader is referred to the web version of this article.)

Table 3
The NIST tabulated values for the considered atomic (I) or ionic (II) element lines, the first ionization energy E∞ and the measured relative spectral response S_R of the used LIBS apparatus.

Element	State	Wavelength (nm)	g_kA_{ki} (10^8 s^{-1})	E_k (eV)	E_i (eV)	E_∞ (eV)	S_R
Al	I	226.35	2.73e+00	5.476	0.000	5.986	15
Ba	II	493.41	1.91e+00	2.512	0.000	5.212	535
Ca	I	422.67	6.54e+00	2.934	0.000	6.113	201
Ca	I	443.50	3.4e+00	4.681	1.886	6.113	240
Cr	I	425.46	2.83e+00	2.913	0.000	6.766	205
Cr	I	520.84	3.52e+00	3.321	0.941	6.766	527
Cu	I	327.40	2.75e+00	3.786	0.000	7.726	66
Cu	I	515.32	2.4e+00	6.191	3.786	7.726	530
Fe	I	404.58	7.76e+00	4.548	1.485	7.902	131
H	I	656.28	7.94e+00	12.087	10.199	13.598	421
K	I	769.90	7.47e-01	1.610	0.000	4.341	1000
Li	I	670.78	1.48e+00	1.848	0.000	5.392	558
Mg	I	285.21	1.47e+01	4.346	0.000	7.646	45
Mg	I	518.36	1.68e+00	5.108	2.717	7.646	527
Mn	I	403.08	1.4e+00	3.075	0.000	7.434	125
Na	I	330.24	1.10e-01	3.753	0.000	5.139	65
Na	I	589.59	1.23e+00	2.102	0.000	5.139	532
Pb	I	405.78	2.7e+00	4.375	1.320	7.417	132
Si	I	288.16	6.51e+00	5.082	0.781	8.151	47
Si	II	634.71	2.34e+00	10.074	8.121	8.151	444
Sr	II	407.77	5.64e+00	3.040	0.000	5.695	135
Ti	I	499.11	6.42e+00	3.319	0.836	6.828	542
V	I	437.82	1.38e+01	3.131	0.286	6.746	230
Zn	I	213.86	2.14e+01	5.796	0.000	9.394	9
Zn	I	481.05	–	6.654	4.079	9.394	489

$$N_e\left[cm^{-3}\right] = 10^{17} \bullet \left(w_{SA}[nm]/1.098\right)^{1.47135} \tag{2}$$

Where w_{SA} is the half-width (nm) at half area of the Hα line profile, that could be approximated as $w_{SA} \approx w_S$.

Across the investigated range on ST21#W (0–500 pg of element mass), the apparent N_e remains constant within the measuring uncertainty, with value of $1.4 \bullet 10^{17}$ cm^{-3}. The expected increase in N_e with sample mass due to easily ionizing elements in sample was not evident because of a relatively large error in the estimation (> 20%) and very small sample mass. Due to the long integration time of the detectors (30 μs) and fast decay of the H_α line originating from a high excitation level, the actual N_e is certainly lower than the here retrieved value. The plasma temperature was evaluated through the Boltzmann's plot involving seven Ti I lines listed in Table S1 (Supplementary material), where it was possible to track the plasma temperature down to the element mass of 50 pg. Although the measuring errors here must be considered large, there is a clear trend shown in Fig. 2c that indicates the temperature decay with the wafer coverage. This trend was further confirmed by measuring the peak ratio RSi of the Si II and Si I lines (Fig. 2d), as an indicator of the plasma temperature [28], where the initial fast drop is followed by a slower decay starting from 100 pg of element mass. As the implications of these results, we must consider that the LIBS probing of trace samples placed on wafer produces a more intense and hotter plasma when reducing the sample mass inside the laser spot, so the optimal signal intensity is a compromise between the ablated sample mass and substrate coverage. In any case, calibrations for semi-quantitative element determinations here, must consider changes in the plasma temperature inside a certain range while some small fluctuations in the electron density are also expected.

Assuming that the plasma is in Local Thermal Equilibrium (LTE) during the detection window and that the plasma is formed of electrons, atoms and single ionized species, the ratio of ionic and atomic number densities of elementt α depends on plasma temperature T and electron density N_e through Saha equation:

$$\frac{N_\alpha^{II}}{N_\alpha^{I}} = \frac{1}{N_e}\cdot\frac{U_\alpha^{II}(T)}{U_\alpha^{I}(T)}B(kT)^{3/2}e^{-\frac{E_\infty}{kT}} \tag{3}$$

where: N_α^I and N_α^{II} are number densities of neutral and ionized element's species, respectively, $U_\alpha^I(T)$ and $U_\alpha^{II}(T)$ are partition functions of atomic and the first ionization stage, respectively; E_∞ is the effective ionization energy in the plasma surrounding; k is Boltzmann constant, B is a constant which numeric value was calculated to be 6.05E+21 cm^{-3} [10].

For Mg and Ca, the theoretical atomic fractions as a function of plasma temperature were calculated for three different electron densities (Figs.3a-b). Due to a lower ionization energy of atomic Ca (6.113 eV) compared to Mg (7.646 eV), the temperature increase above 5500 K leads to a rapid loss of Ca atoms due to ionization, whereas Mg is depleted above 6000–6500 K, dependently on the electron density.

For the plasma in LTE, neglecting re-absorption effects of plasma emission, the spectrally integrated line intensity corresponding to the atomic or ionic transition between levels E_k and E_i of the element α is given by:

$$I^{ki}{}_\alpha = a'_\alpha N_\alpha \frac{g_k A_{ki} e^{-E_k/kT}}{U_\alpha(T)} \tag{4}$$

where a'_α is a constant depending on experimental conditions.

From the theoretical simulations based on eq. (3) and eq. (4), the ratio of lines Mg I at 518.36 nm and Ca I 443.50 nm varies strongly with plasma temperature in the considered range, particularly for lower electron densities (Fig. 3c). From this point of view, the optimal conditions for the quantitative LIBS analysis of elements with very different ionization energies as in the reported example, regard relatively low plasma temperatures, for example, between 5500 K and 6500 K. On the other hand, measuring of the relative content of elements with mutually close ionization energies, like Mg (7.646 eV) and Fe (7.902 eV), particularly through the lines with similar excitation levels, is weakly influenced by variations both in plasma temperature and electron density (Fig. 3d). For multi-elemental LIBS analysis, the mutual variability of the line intensities could be reduced by optimizing the acquisition delay towards lower plasma temperatures while still maintaining the line intensities i.e. detection sensitivities reasonable high. Analytical lines with similar excitation levels [36] should be prioritized, but in practice, only a limited number of intense, interference-free transitions might be available in some sample types. Resonant lines of major constituents should be avoided whenever possible due to self-absorption and saturation.

Basing on the earlier considerations, we examined the mutual

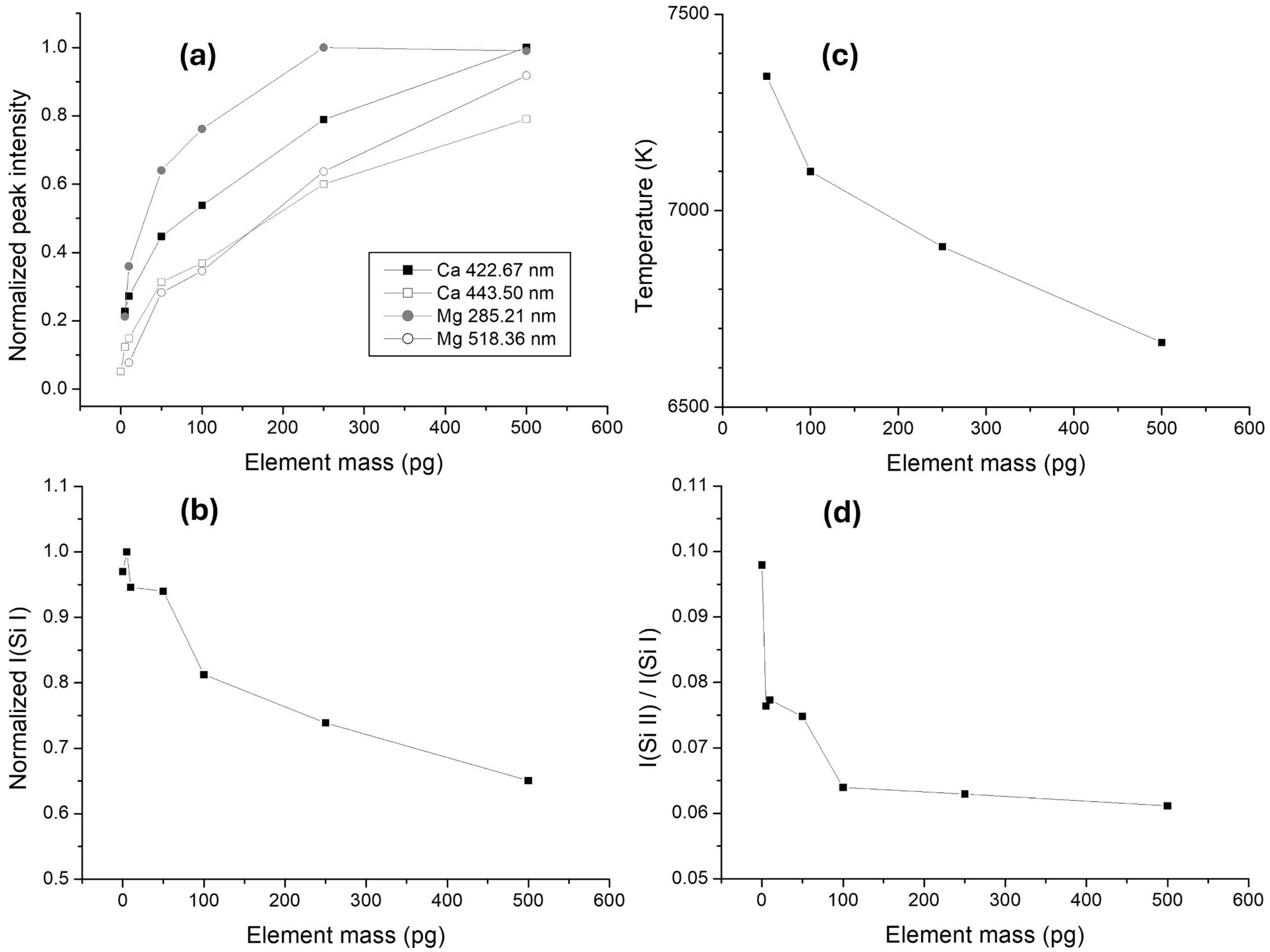

Fig. 2. Effect of the element mass for ST21#W sample, on: (a) Normalized peak intensities from Ca I and Mg I; (b) normalized peak intensity of Si I (288.16 nm); (c) estimated plasma temperature; (d) Measured peak ratio of Si II at 634.71 nm and Si I at 288.16 nm.

behaviour of Mg I peak at 518.36 nm and Ca I peak at 443.5 nm, measured on ST21#W and Rock#W samples. Both peaks had stable linewidth (obtained from the line fitting) with changing the sample mass inside the laser spot, leading us to a conclusion that that these transitions were not self-absorbed in our experimental conditions. For ST21#W, the spectra averaged over six measurements per each sample mass produced narrow histograms of the Si II/Si I ratio (RSi), which is exploited as a plasma temperature indicator (Fig. 4a). Only spectra from the clean substrate showed high RSi value. In contrast, the spectra acquired on Rock#W showed a much wider distribution of RSi (Fig. 4b). For ST21#W, Mg intensity scaled linearly with Ca peak, with a negative intercept (Fig. 4c, Table 4); note that on clean substrate Mg and Ca peaks were absent. For Rock#W, the Mg(Ca) linear dependency had a positive intercept (Fig. 4d).

To distinguish Mg(Ca) dependency on the plasma temperature, here indirectly monitored through RSi, for the Rock# particles we separated the calibration graphs into two parts: for RSi < 0.06 and RSi ≥ 0.06 (Fig. 5). This limit was selected to have a similar number of the data points on both sides: 6 points with RSi < 0.06 and 8 points with RSi ≥ 0.06. In the first case, the linear fit produced high positive value of the intercept *A* while for high RSi ratios the intercept *A* is close to zero (Table 4). The electron density measured on the rock particles varied between $1.3 \cdot 10^{17}$ cm^{-3} and $2.2 \cdot 10^{17}$ cm^{-3} where the increase in N_e was observed at lower temperatures, corresponding to higher sample masses inside the laser spot; here, a significant presence of elements with low ionization energy (e.g. K, Na and Al) in the rock material contributes to release of electrons to the plasma. The results of the linear fits of Mg(Ca) for ST21#W and Rock#W are summarized in Table 4 where we considered two types of calibration coefficients, namely c_B - through the linear slope *B* of the growth Mg(Ca), and c_R - through the peak ratio Mg/Ca.

Here we define the calibration coefficient c_{el} for one element as a multiplier for the corresponding peak intensity that would bring the concentration ratio (%wt el):(wt% Ca) in sample equal to 1:1.

$$c_{el} = d_{el} \bullet \frac{wt\%Ca}{wt\%el} \tag{5}$$

where d_{el} is dependency found experimentally for one selected element line on the chosen Ca peak (443.50 nm), and it was calculated in two ways:

1) as c_B - corresponding to d_{el} equal to the linear slope from the plot I_{el} (I_{Ca}).

2) c_R - corresponding to d_{el} calculated as the peak ratio I_{el}/I_{Ca}.

In case of sample ST21, where all certified elements have the same mass, the calibration coefficient c_{el} is equal to d_{el}.

The results reported in Table 4 confirm that the slope Mg(Ca) increases with the plasma temperature i.e. with RSi, while the intercept is reduced, as expected from the theoretical simulations (see Fig. 3). In the examined case, the relative differences between the derived calibration coefficients c_B for the two samples were between 25% and 37%,

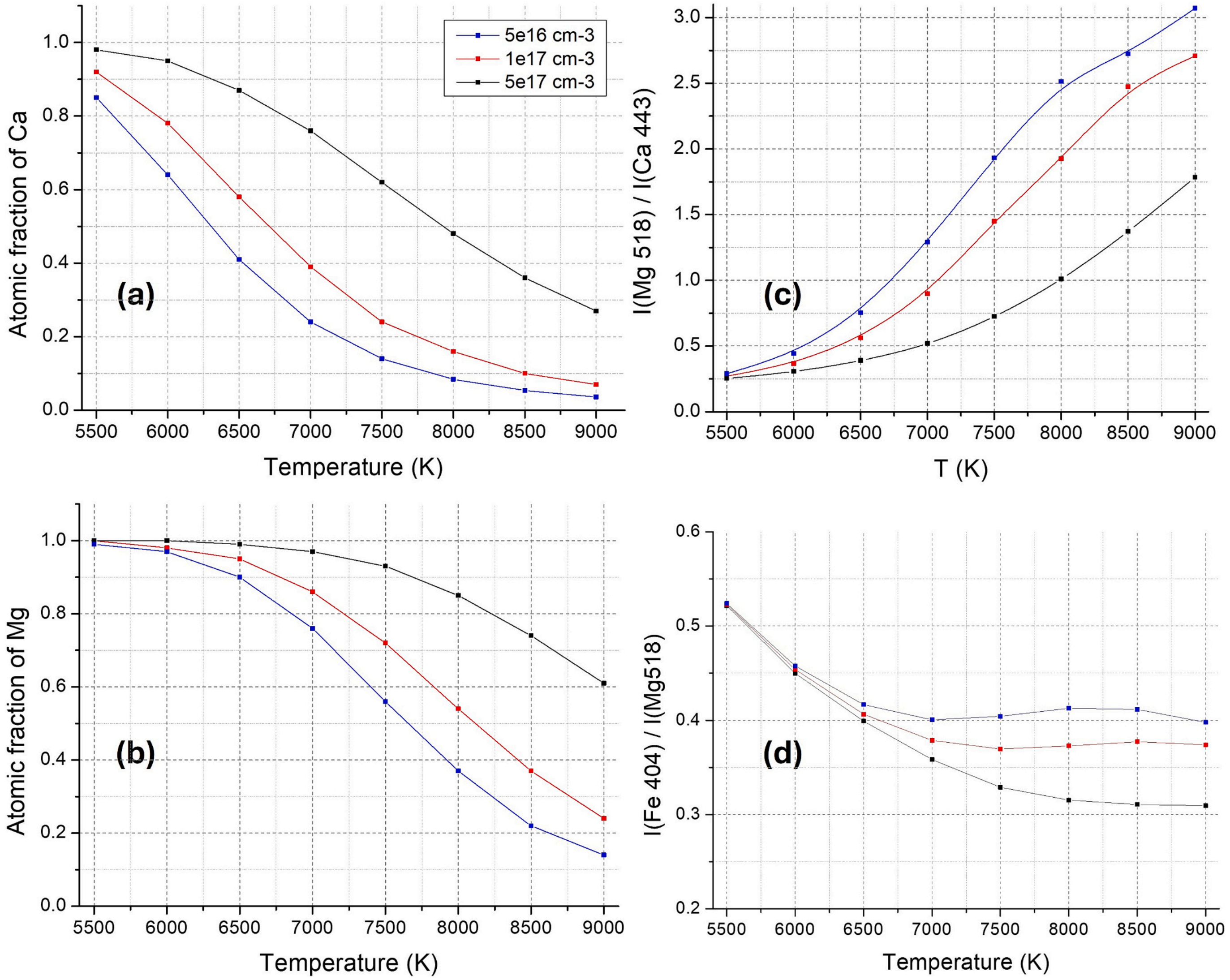

Fig. 3. Theoretical values with the plasma temperature, of atomic fractions of Ca (a) and Mg (b); line ratio of Mg I at 518.36 nm and Ca I at 443.50 nm (c), line ratio of Fe I at 404.58 and Mg I at 518.36 (d). The calculations regard the plasma electron densities of $5{\bullet}10^{16}$ cm^{-3} (blue), $1{\bullet}10^{17}$ cm^{-3} (red) and $5{\bullet}10^{17}$ cm^{-3} (black) where the data between the simulated temperatures (dots) are extrapolated. (For interpretation of the references to colour in this figure legend, the reader is referred to the web version of this article.)

depending on the RSi that is an indirect indicator of the plasma temperature. These differences in the calibration coefficients can be considered satisfactory in semi-quantitative LIBS analysis on samples with very different compositions: in the specific case, Mg concentration is 4.76% and 1.04% in ST21# and Rock#, while the certified Mg/Ca concentration ratio changes from 1 to 0.28, respectively. Furthermore, on sample Rock# we found that the electron density decreases with the plasma temperature, the effect not observed on ST21 sample. On the other hand, the calibration coefficients $c_{R,}$ through the peak ratio, differ between 56% and 60% for the two samples. In this case, changes in the plasma parameters are reflected through the linear intercept A in dependency Mg(Ca), that might assume both negative and positive values. Considering this, a robust calibration should be based on experimentally induced changes in the line intensities, sufficient to determine the mutual growth coefficient for two analytical peaks [31].

The previously analysed case regards a not resonant Mg I line where the peak's linewidth was constant, inside the fitting error, in all considered spectra. For resonant transitions, usually exploited for detecting trace elements, an occurrence of self-absorption is expected. On ST21#W sample, containing 4.76% of Cr, the width of Cr I peak at 425.46 nm increases already when passing from 5 pg to 10 pg of the element's mass (Fig. 6a). The presence of strong self-absorption here precludes a possibility for calibration, even if considering the peak integral instead of its height (Fig. 6b). Differently, sample Rock# contains only 32 ppm of Cr, and self-absorption of the same Cr I peak was not observed except in two most intense spectra in the data set. After excluding these two points as outliers, on Rock#W we obtained a satisfactory linear calibration (Fig. 6c). We also examined an intense not resonant Cr I peak at 520.84 nm, although it is not well isolated and requires multiple peak fitting or approximate evaluation of its height (Fig. S2, Supplementary material), where both approaches are to be considered with a significant error in estimation. For this Cr I transition, on ST21#W sample dependency Cr(Ca) is well approximated by the linear growth up to 100 pg of the element mass (Fig. 6d).

3.2. Calibration coefficients

For nine calibration samples, listed in Table 1, we analysed dependency of the fitted element peak heights on the Ca I peak at 443.50 nm. Except some spectra from BaCa#W sample, discarded due to highly intense and saturated peaks, the reference Ca line showed no changes in linewidth. In the calibration plots, points affected by saturation for high

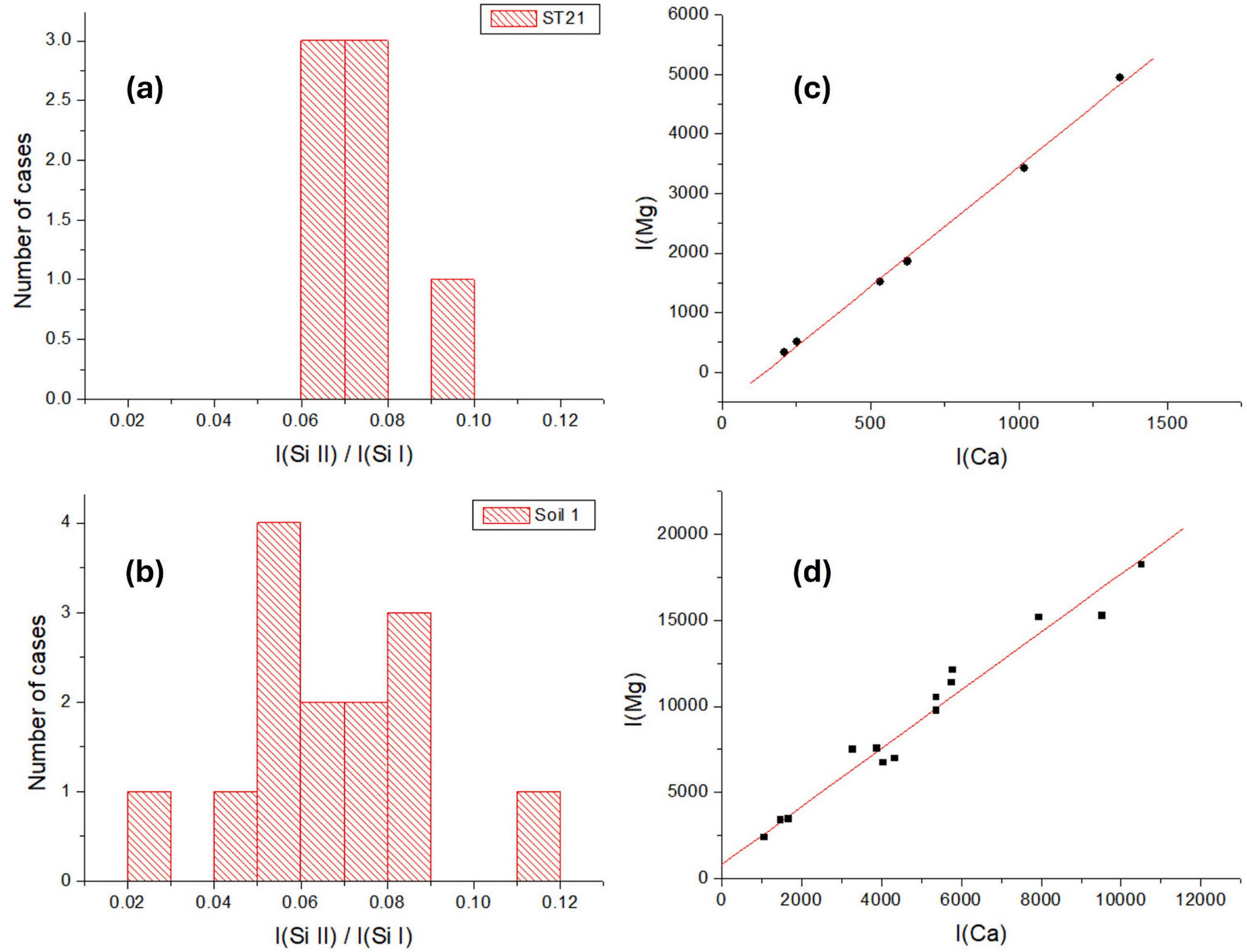

Fig. 4. Histogram relative to the ratio RSi for: (a) the spectra averaged per ST21#W mass and for clean substrate; (b) single shot spectra on Rock1#W. The corresponding dependencies of Mg I line peak at 518.36 nm and Ca I at 443.50 nm are shown in (c) and (d), respectively.

Table 4

Comparative results of linear fit Mg (Ca) and calibration coefficients c_B and c_R for samples ST21#W and Rock#W, considering Mg I at 518.36 nm and Ca I at 443.50 nm.

	ST21#W	Rock#W all points	Difference	Rock#W RSi < 0.06	Difference	Rock#W RSi > 0.06	Difference
Mg/Ca %wt	1.0	0.28	–	0.28	–	0.28	–
R Pearsons's	0.999	0.982	–	0.965	–	0.998	–
Intercept A	−576 ± 77	1036 ± 522	–	1664 ± 1254	–	446 ± 212	–
c_B	4.13 ± 0.10	5.90 ± 0.36	30%	5.50 ± 0.67	25%	6.57 ± 0.17	37%
c_R	2.91 ± 0.77	6.94 ± 0.92	58%	6.61 ± 0.95	56%	7.23 ± 0.59	60%

spectral intensities were excluded from linear fitting (see Fig. 6d).

On ST21#W, where all element concentrations are equivalent to 4.76%, the curve bending was already observed above the element mass of 10 pg for following transitions: Cr I at 425.46 nm, Cu I at 327.40 nm, Mn I and Sr II. In such cases, calibration on ST21#W involved only two points and so retrieved values are only indicative. Besides this sample, departure from the linear growth of the line peaks versus Ca peak (saturation) was frequently observed for resonant lines from Na, K and Al, then for Cu, Cr and Mn peaks in case of their high loads in samples, then for Fe peak in Ash#W that contains 9.4% of this element, and for Sr in some very intense spectra from various samples.

Calibration coefficients for each analytical line were derived in two ways: (i) from the slope of linear fits (c_B), and (ii) from peak ratios (c_R). In some cases of low element concentrations, some weak analytical lines were not detected in a sufficient number of spectra to determine reliable slopes. Importantly, these coefficients are correction factors: dividing the measured slope or intensity by the coefficient, normalizes the elemental concentration to that of Ca. For example, when using line ratios, each peak is divided by its calibration coefficient c_R, where $c_R = 1.0$ is adopted for the Ca peak. Correction of the measured analytical peaks by here supplied coefficient can be further exploited to bring the concentrations of all detected elements, in free or in known forms (e.g. specific oxides), to the presumed sum, for example to 100%. This approach is analogue to the calibration free method and allows the semi-quantitative estimation of the element abundances. Another way to retrieve absolute concentrations of other elements in sample and within

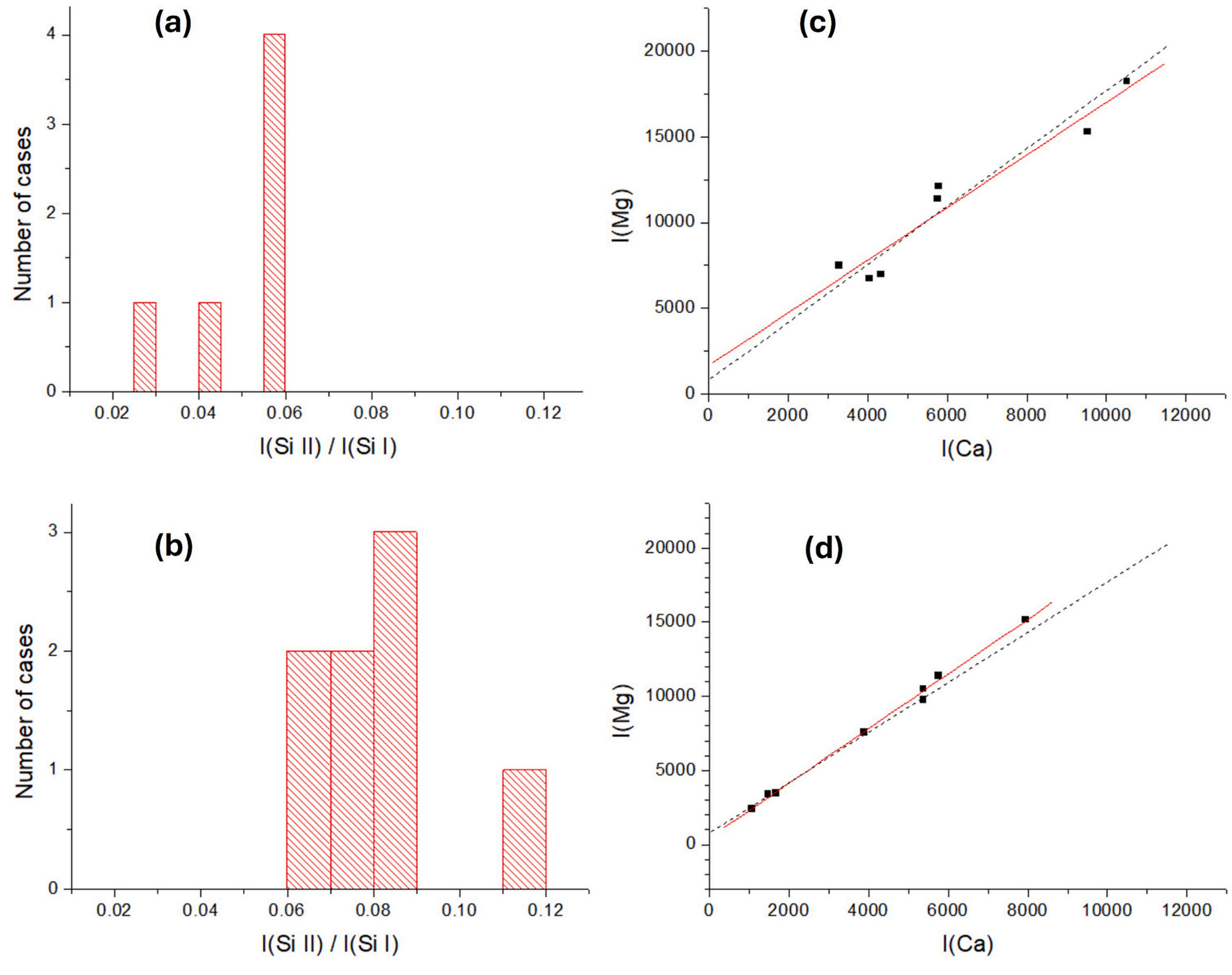

Fig. 5. Histograms relative to the ratio RSi for the spectra on Rock#W with RSi < 0.06 (a) or RSi ≥ 0.06 (b), and the corresponding dependencies of Mg I line peak at 518.36 nm and Ca I at 443.50 nm (c) and (d), respectively where the linear fit corresponding to all RSi values (dot line) is shown for comparison.

certain limits, is through the initial knowledge of the Ca concentration that could come from other measuring techniques (e.g., from XRF) or from the predicted presence of Ca in certain samples (e.g., calcareous rocks).

The calculated calibration coefficients c_B and c_R for each detected element in the samples are reported in Tables S2-S3 (Supplementary material), together with the known element concentrations. The reported differences in these two coefficients, if exceeding the measurement error, indicate that the Intercept A is departing from zero value for the given element transition and concentration in sample.

In an ideal case, the calibration coefficients should be constant over all possible element concentrations. Unfortunately, in real conditions this is not the case, and calibrations are usually performed and valid inside limited concentration ranges. In optical emission techniques, weaker element transitions are preferable for higher element concentration range while low element abundancies are usually measured through the intense (often resonant) transitions.

Behaviour of the calibration coefficients with element concentrations i.e. samples, is shown in Fig. 7 for Al, Ba, Cu and Cr. The first general observation is that c_B values (slope-based) vary less across the concentration range than c_R values (ratio-based); moreover, their measurement errors are also smaller. Secondly, c_R values, if not also c_B coefficients, tend to decrease towards high element concentrations, especially for resonant transitions; this effect would lead to the element over-estimation if using the calibration coefficient averaged also over low element concentrations. In case of Al, the chosen resonant transition produced a three-fold decrease in c_R when passing from Al concentration of 0.86% (COAL#W) to 3.6% (Soil4#W). If neglecting fluctuations due to residual matrix effect and errors from various sources like peak fitting and linear growth approximation, coefficient c_B for Ba remained essentially constant over extremely wide range of concentrations, from 68 ppm (COAL#W) to 34.8% (BaCa#W). Differently, changes in c_R are evident at two extreme Ba concentrations while in the middle, the values are inside the estimated errors per sample. For both considered Cr I lines, c_B could be approximated as constant in range 32–200 ppm, but the c_R value rapidly increases towards low Cr concentrations, making the quantitative estimation through the line ratio very uncertain. Note that the value c_B for Cr I transition at 425.46 nm on ST21#W is only indicative, being deduced from only two calibration points. Calibration for Cu required two ranges: below 200 ppm and above 0.3%, where on unknown samples, we suggest the use of the second range if a relatively weak Cu I line at 515.32 nm is detected.

Another set of calibration coefficients as a function of element concentration in samples, is shown in Fig. 8. The selected lines of Fe and Mg show almost constant calibration coefficient c_B over the whole examined range, i.e. 0.76% - 9.4% and 0.038%–4.8%, respectively. The

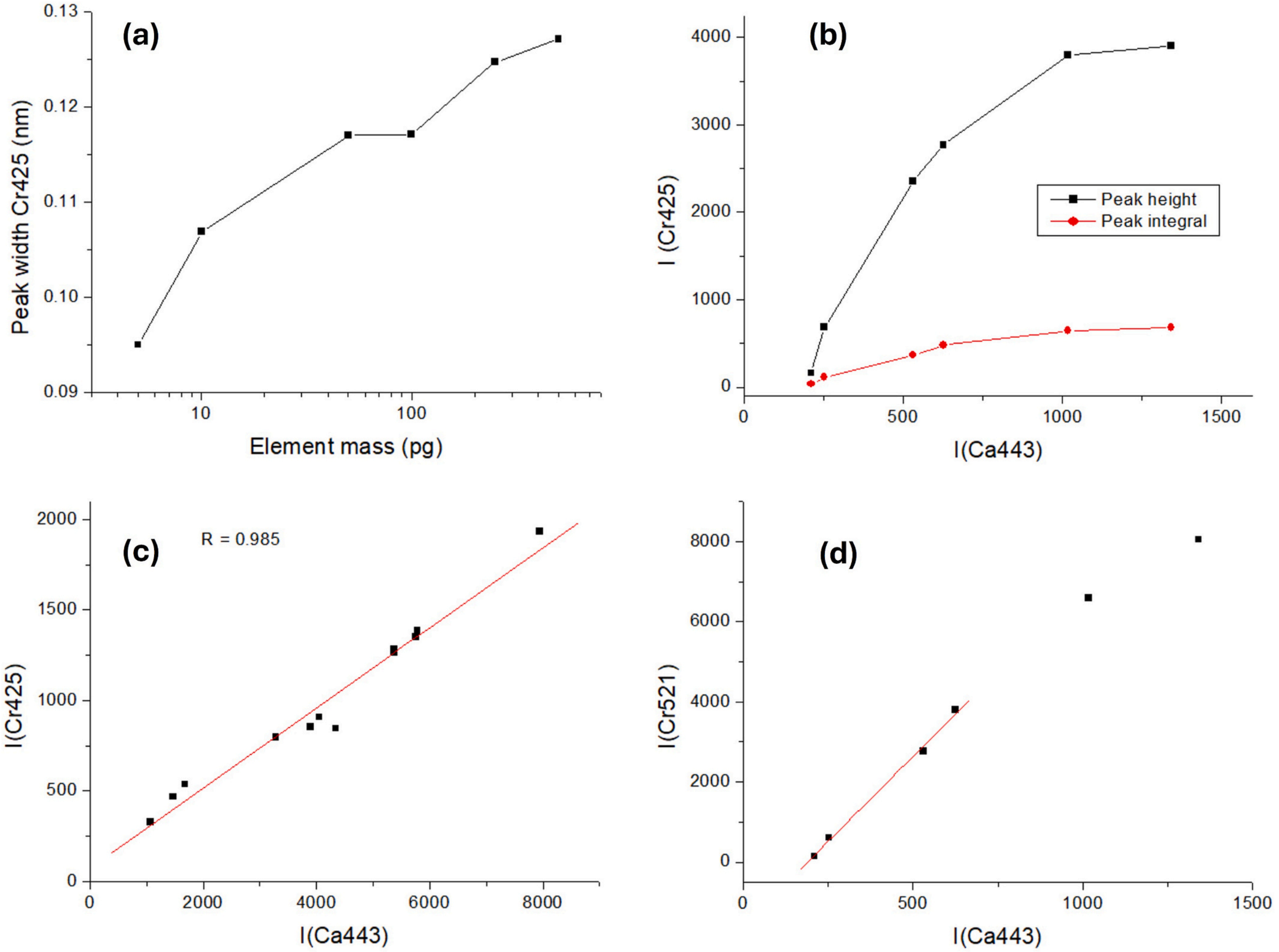

Fig. 6. (a) Peak width of resonant Cr I line at 425.46 nm as a function of the element mass in sample ST21#W. (b) Height (black) and area (red) of resonant Cr I peak at 425.46 nm as a function of peak height from Ca I at 443.50 nm, in sample ST21#W. (c) Height of resonant Cr I peak at 425.46 nm as a function of peak height Ca I at 443.50 nm, in sample Rock#W. (d) Height of Cr I peak at 520.84 nm as a function of peak height from Ca I at 443.50 nm, in sample ST21#W. (For interpretation of the references to colour in this figure legend, the reader is referred to the web version of this article.)

coefficients for Mn differ only for the maximum element concentration (sample ST21); both calibration coefficients for resonant K and Na lines show the previously observed decrease towards high element concentrations.

Further examples of the calibration coefficients are depicted in Fig. 9. Despite some scattered points, calibration for Sr and Ti through c_B could be approximated as constant over the entire range, namely 0.045% - 4.8% and 0.013% - 4.8%, respectively. Pb and V showed the almost stable coefficients in range 72 ppm - 5500 ppm and 54 ppm - 300 ppm, respectively. Calibration for Zn through the peak at 481.05 nm was stable between 220 ppm and 4200 ppm while the resonant Zn I line at 213.86 nm showed strong concentration dependency, particularly regarding the c_R values.

For Li, certified concentrations were available only in three samples. Nevertheless, the Li I 670.78 nm line showed that calibration coefficients decreased even by a factor of ~100 when concentration increases from 28 ppm to 4.8% (Table S2, Supplementary material).

Following these analyses, we extrapolated the calibration coefficients c_B (Table 5) and c_R (Table 6) specifying the tested calibration ranges or specific values. We point out that points (spectra) corresponding to saturation of the analytical line i.e. departure from the linear fit, were excluded from the calibration. Coefficients for Si, obtained from one soil sample on an Al substrate, are also included in Tables 5–6, though only as indicative values.

In the Tables above, we omitted Na I peak at 330.24 nm because it resulted overlapped with an intense Zn I line at 330.26 nm, the element present in high concentration (0.42%wt) in sample Soil#2.

3.3. *Application of the calibration coefficients for semi-quantitative sample analysis*

The first sample selected for validation was Soil2#, which element concentrations are shown in Fig. 10a. In the initial calibration, this sample was included through the measurements on particles placed on aluminium substrate. In the validation phase, however, Soil2# was analysed as particles on wafer, where the spectral intensities are lower than on aluminium. For validation, 18 single shot spectra were collected, and both the linear slope B_{el} of the element peak vs. Ca peak, and the averaged peak ratio I_{el}/I_{Ca} was calculated. To evaluate the method's analytical capability, the Ca was assumed to be initially known, corresponding to the certified concentration (CC_{Ca}) of 0.964%. Element concentrations were then calculated as:

$$C_{el} = \frac{B_{el}}{c_B} \bullet CC_{Ca} \tag{6}$$

Or as:

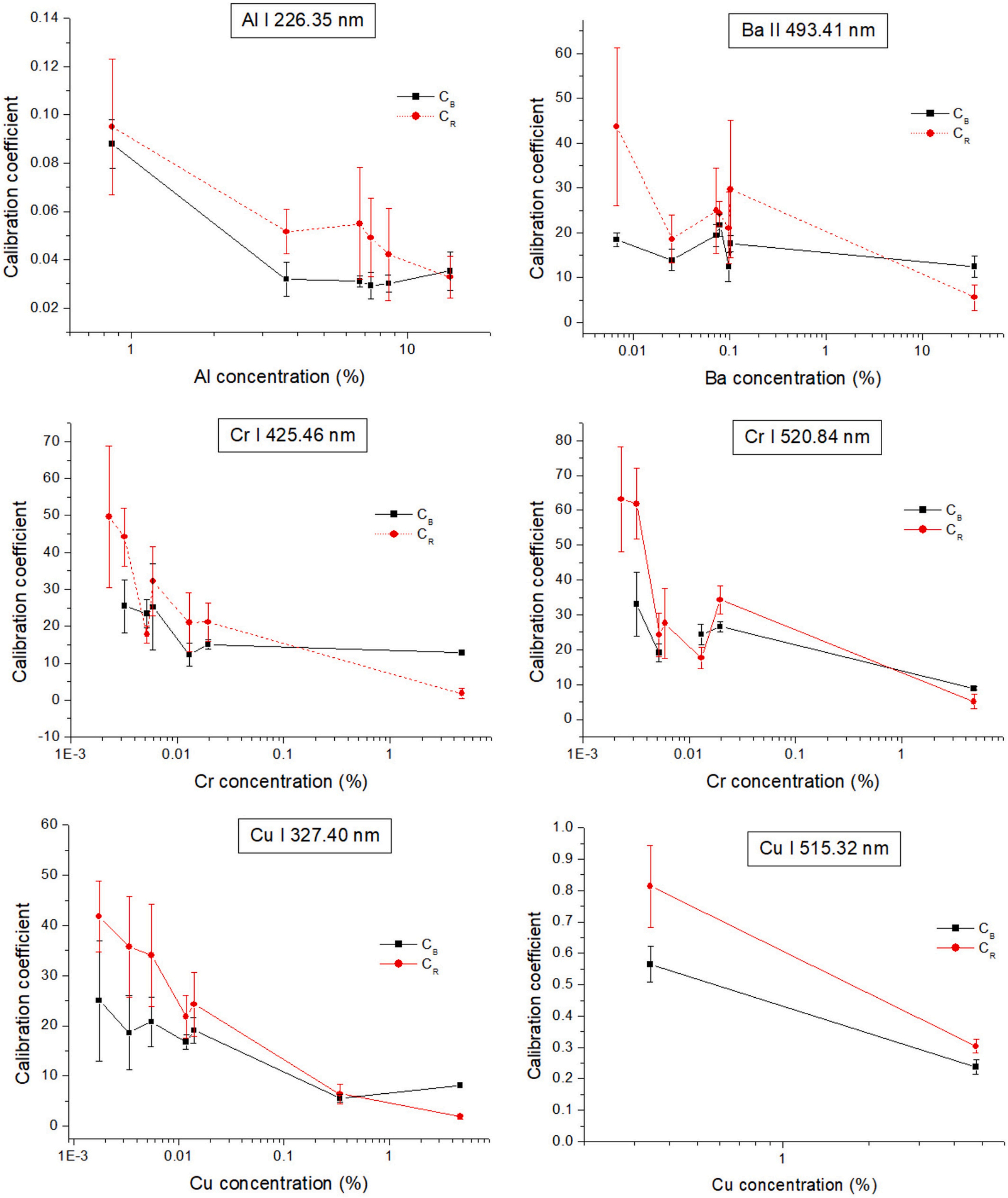

Fig. 7. Calculated calibration coefficients c_B (black) and c_R (red) as a function of element concentration in samples for Al, Ba, two Cr and two Cu lines. (For interpretation of the references to colour in this figure legend, the reader is referred to the web version of this article.)

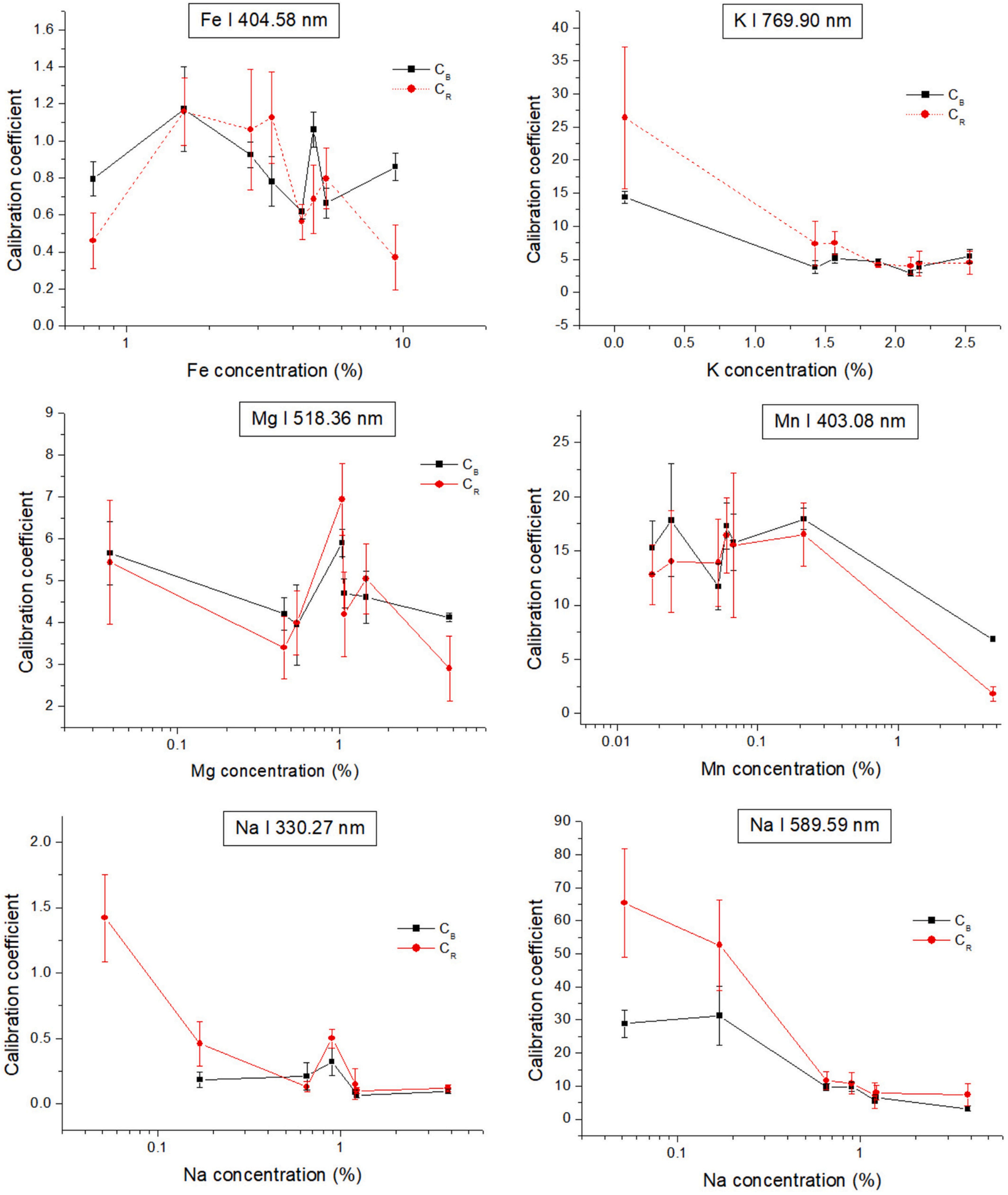

Fig. 8. Calculated calibration coefficients c_B (black) and c_R (red) as a function of element concentration in samples for Fe, K, Mg, Mn and two Na lines. (For interpretation of the references to colour in this figure legend, the reader is referred to the web version of this article.)

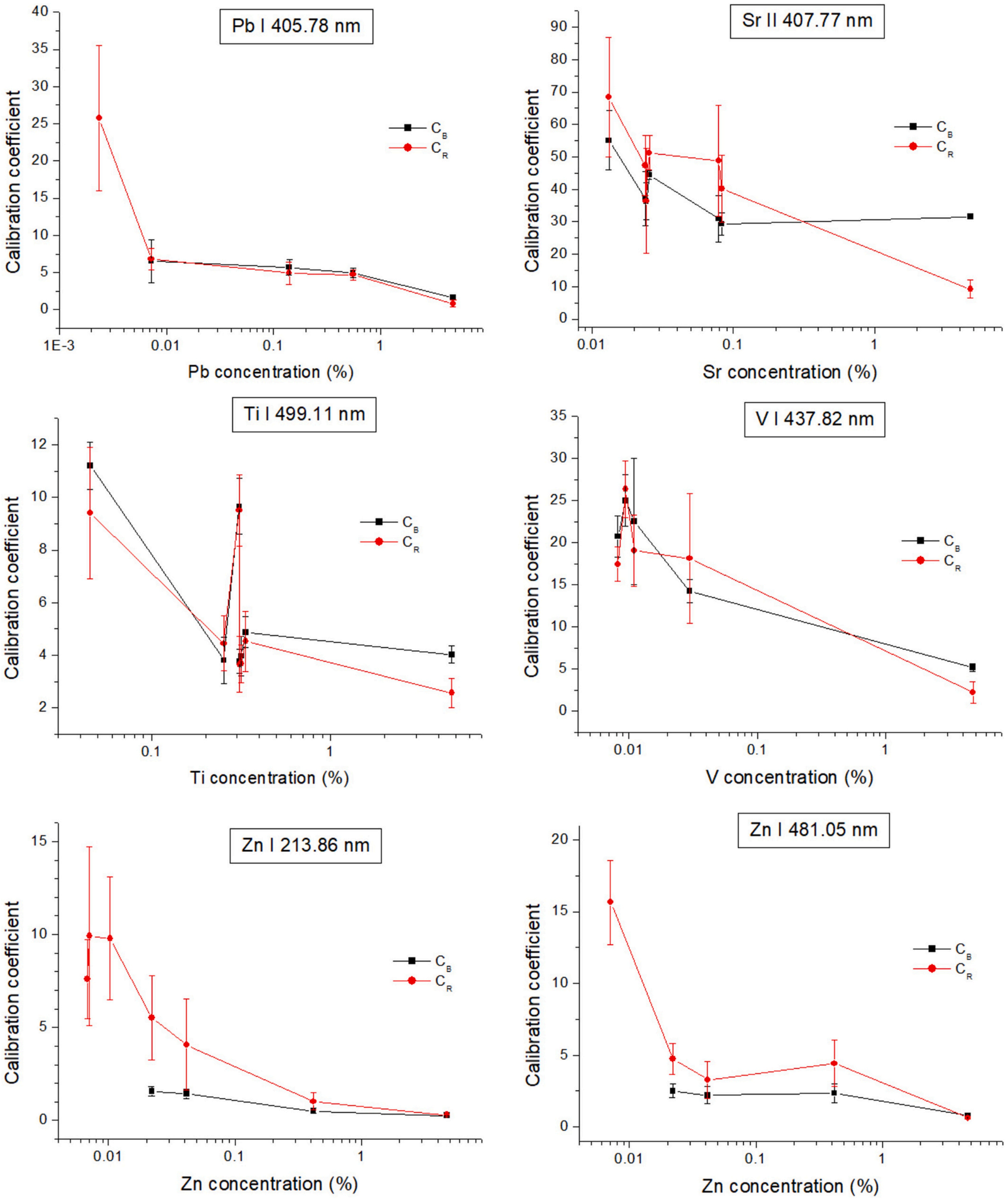

Fig. 9. Calculated calibration coefficients c_B (black) and c_R (red) as a function of element concentration in samples for Pb, Sr, Ti, V and two Zn lines. (For interpretation of the references to colour in this figure legend, the reader is referred to the web version of this article.)

Table 5

Calibration coefficients c_B averaged over different samples inside the specified concentration ranges or a mean value over multiple measurements on one sample.

Element	Peak (nm)	Concentration 1	c_B	Concentration 2	c_B
Al	226.35	3.6% - 14.3%	0.0315 ± 0.0024	≈0.86%	0.088 ± 0.012
Ba	493.41	68 ppm - 35%	16.5 ± 3.7		
Cr	425.46	32 ppm - 4.8%	20.8 ± 6.1		
Cr	520.84	32 ppm –200 ppm	22.8 ± 5.8	≈4.8%	8.8 ± 0.5
Cu	327.40	18 ppm – 140 ppm	20.0 ± 3.1	0.34% - 4.8%	5.6 ± 0.7
Cu	515.32	≈0.34%	0.56 ± 0.07	≈4.8%	0.237 ± 0.022
Fe	404.58	0.8% - 9.4%	0.86 ± 0.19		
K	769.90	≈750 ppm	14.3 ± 0.95	1.4% - 2.5%	4.30 ± 0.94
Li	670.78	18 ppm – 28 ppm	1120 ± 80	≈4.8%	13.6 ± 2.1
Mg	518.36	380 ppm - 4.8%	4.73 ± 0.76		
Mn	403.08	180 ppm – 2100 ppm	16.0 ± 2.4	≈4.8%	1.80 ± 0.64
Na	589.59	0.052%–0.17%	30.1 ± 1.7	0.65% - 3.9%	7.0 ± 2.8
Pb	405.78	72 ppm – 550 ppm	5.73 ± 0.79	≈4.8%	1.65 ± 0.11
Si	288.16	≈31%	1.49 ± 0.16		
Sr	407.77	130 ppm-4.8%	37.8 ± 9.2		
Ti	499.11	450 ppm - 4.8%	5.9 ± 3.1		
V	437.82	82 ppm – 300 ppm	20.6 ± 4.5	≈4.8%	5.20 ± 0.42
Zn	213.86	220 ppm – 420 ppm	1.49 ± 0.10	0.42% - 4.8%	0.38 ± 0.17
Zn	481.05	220 ppm – 4200 ppm	2.36 ± 0.15	≈4.8%	0.790 ± 0.037

$$C_{el} = \frac{\frac{I_{el}}{I_{Ca}}}{c_R} \bullet CC_{Ca} \tag{7}$$

Where c_B and c_R values were taken from Table 5 and Table 6, respectively.

The relative difference between the measured and certified values was estimated as:

$$\Delta C = \frac{C_{el} - CC_{el}}{CC_{el}} \tag{8}$$

Where CC_{el} is the certified element concentration.

As previously discussed, larger discrepancies are expected when using the line-ratio method compared to the slope-based method because: (i) the line ratio is more sensitive to the eventual peak saturation while the linearly approximated slope encompasses the data points corresponding to various sample masses and line saturation degrees (if present); (ii) variations of the plasma parameters strongly affect the line ratio, mainly through the variable intercept in mutual dependency of the analytical and the normalizing line (here Ca I at 443.50 nm) while the corresponding slope exhibits minor changes. This was confirmed through comparative errors ΔC for various elements (Figs.10b-c). For the concentration measurements through the slope, with coefficients given in Table 5, only Zn concentration, here measured though peak at 481.05 nm, exceeds error of 0.3 (Zn is overestimated for about 40%). In case of Cr, the error ΔC was of −0.03 and + 0.16 for the peaks at 425.46 nm and 520.84 nm, respectively. For the element concentrations measured through the line ratios, with coefficients given in Table 6, the error ΔC exceeds +0.5 for Al, Na and Cr while the error for Mn approaches this limit. The errors below ±0.3 remained for the retrieved concentrations of Fe, K, Mg, Pb, Zn, Ti, Ba and Sr.

Table 6

Calibration coefficients c_R averaged over different samples inside the specified concentration ranges or a mean value over multiple measurements on one sample.

Element	Peak (nm)	Concentration 1	c_R	Concentration 2	c_R
Al	226.35	3.6–14.3%	0.046 ± 0.009	≈0.86%	0.095 ± 0.028
Ba	493.41	68 ppm –1000 ppm	27 ± 9	≈35%	5.6 ± 2.9
Cr	425.46	23 ppm –200 ppm	31 ± 13	≈4.8%	1.7 ± 1.4
Cr	520.84	52 ppm –200 ppm	25.9 ± 7.0	≈4.8%	5.1 ± 2.1
Cu	327.40	18 ppm – 140 ppm	31.5 ± 8.3	≈0.34%	6.4 ± 2.0
Cu	515.32	≈0.34%	0.81 ± 0.13	≈4.8%	0.304 ± 0.021
Fe	404.58	0.8%–9.4%	0.78 ± 0.31		
K	769.90	≈750 ppm	26 ± 11	1.4% - 2.5%	5.30 ± 1.6
Li	670.78	18 ppm – 28 ppm	1100 ± 140	≈4.8%	14.1 ± 1.2
Mg	518.36	380 ppm - 4.8%	4.6 ± 1.4		
Mn	403.08	180 ppm – 2100 ppm	14.9 ± 1.5	≈4.8%	1.78 ± 0.64
Na	589.59	0.052%– 0.17%	59.0 ± 9.0	0.65% - 3.8%	9.0 ± 2.0
Pb	405.78	≈24 ppm	25.6 ± 9.8	72 ppm – 550 ppm	5.5 ± 1.2
Si	288.16	31%	1.65 ± 0.28		
Sr	407.77	130 ppm – 830 ppm	49 ± 11	≈4.8%	9.2 ± 2.8
Ti	499.11	450 ppm - 4.8%	5.4 ± 2.8		
V	437.82	82 ppm – 300 ppm	20.2 ± 4.1	≈4.8%	2.20 ± 1.3
Zn	213.86	220 ppm – 420 ppm	4.8 ± 1.0	≈0.42%	1.01 ± 0.46
Zn	481.05	≈71 ppm	15.6 ± 2.9	220 ppm - 4200 ppm	4.15 ± 0.76

We also tested Soil2# pressed into a pellet, one year after the initial calibration. The spectral intensities acquired at 10 distanced points on the pellet were similar, preventing construction of calibration graphs based on mutual linear growth of the line intensities. Attempts to reduce the delay to 1200 ns often produced negative slopes of element peak vs. Ca peak, oppositely to the measurements on residues over substrate, here used for calibration. Negative correlation for some element peaks respect to a reference transition (internal standard), has been already seen on bulk samples when changing the incident laser energy over a broad range [37]. Therefore, we averaged the spectra on the pellet and applied the calibration coefficients c_R (Table 6) for element quantifications. In this case, the V peak was too weak to be clearly distinguished. Concentrations retrieved by using Eq. (7) agreed well with certified values for Fe, K, Mg, Pb, Ti, Ba, and Sr (Fig. 10d). The error ΔC was out of scale for both Cr lines ($\Delta C > 1.0$); it is important to note that Cr concentration in Soil2# was the lowest among the examined samples, thus the applied calibration coefficient c_R, averaged over higher concentrations, produced a large over-estimation (see Fig. 8). The calculated abundancies of Cu, Mn and Zn in the pellet are about 50% higher than the certified values, where these three elements have concentrations in Soil#2 for one order of magnitude higher than the other samples

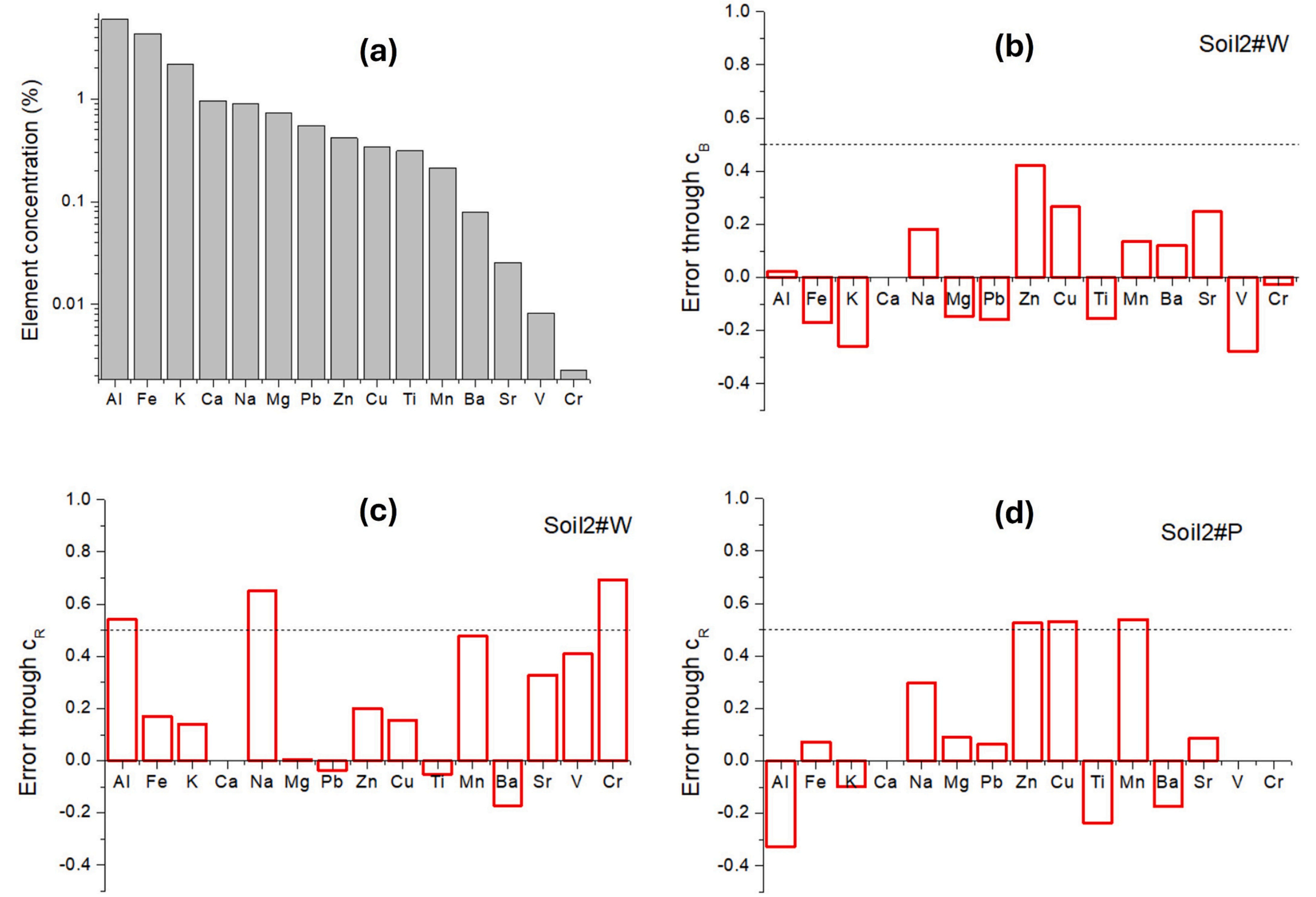

Fig. 10. Certified element concentrations in sample Soil2# (a); errors in determination of the element concentrations through (b) coefficient c_B, and (c) coefficient c_R, for particles on wafer; (d) errors in concentration measurements through coefficient c_R for the soil pressed into pellet. The acquisition delay is 2000 ns.

used to establish the calibration coefficient c_R (See Tables S2-S3, Supplementary material).

On a pellet prepared from Soil#3, which element composition is shown in Fig. 11a and in Tables S2-S3 (Supplementary material), the measured element concentrations through c_R from the spectra acquired with the optimal acquisition delay of 2000 ns, are inside the error of ±0.5, where Al was largely underestimated (Fig. 11b). In this graph we excluded the value for Cr because this element was overestimated with $\Delta C > 1.0$, confirming that both considered Cr lines are inadequate for the concentration measurements through the line ratio over a wide concentration range. To evaluate the effect of mismatching the plasma parameters with respect to the optimal conditions (used for calibration), we varied the acquisition delay. If reducing the acquisition delay to 1700 ns, all measured element concentrations are underestimated (Fig. 11c); further shortening of the acquisition delay down to 1200 ns leads to an increase of the errors ΔC (Fig. 11d) that, however, remain inside the limit of ±0.5 except for Al and Sr. These results confirm that the best prediction accuracy could be achieved for the measurements where the plasma parameters are close to those present during the calibration stage.

From here reported validation results, we might conclude that the calibration through the linear slope among the element's transition and the selected Ca line produces good quantitative results, with error below ±30% for all the considered elements except for Zn. Application of the calibration through the line ratio might lead to larger errors for some elements, particularly for those measured through the resonant lines and/or for the element concentrations close to the extremes of the calibration interval. When passing from the measurements on particles over substrate to the pressed pellets, for similar N_e values the plasma is cooler or for the similar plasma temperatures the N_e is higher (Table 7). A slight mismatching of the plasma parameters affects the concentration measurements that, however, remain inside the error of ±50% for most of the elements (Fe, K, Mg, Ti, Pb, Ba, and Sr). For Al, Cu, Mn, Na and Zn, the retrieved concentrations on pellets might exceed the limit of ±50%, particularly if the real values are close to the limits of the calibration interval. For both considered Cr transitions, the concentration measurements through the peak ratio and over a wide concentration range, is not affordable, as already reported for Cr I line at 425.46 nm [9]. This also means that calibration coefficients for intense resonant lines should be split into more intervals than here, the first one regarding very low element concentrations where self-absorption is still absent.

The discrepancy between the plasma temperature and electron density during the calibration phase and successive concentration measurements, is an important source of errors. The electron density could be controlled through the Stark broadening of H_α line while the temperature indicator RSi is extremely sensitive to the temperature changes in plasma, as deduced from the theoretical simulations (Fig.S3a - Supplementary material). If considering both the peak heights and peak areas for the atomic and ionic Si lines, the measured RSi is much higher than values expected for the plasma temperature around 7000 K because of the spatially integrated acquisition of spectral emission applied in this work. The maximum emission temperatures for atoms and ions differ significantly, depending on the first ionization energy, i. e. in spatially integrated acquisition, where ionic lines are mainly emitted from hotter zones of the plasma. The exact physical meaning of RSi would be found from spatially resolved spectral acquisition, i.e. by

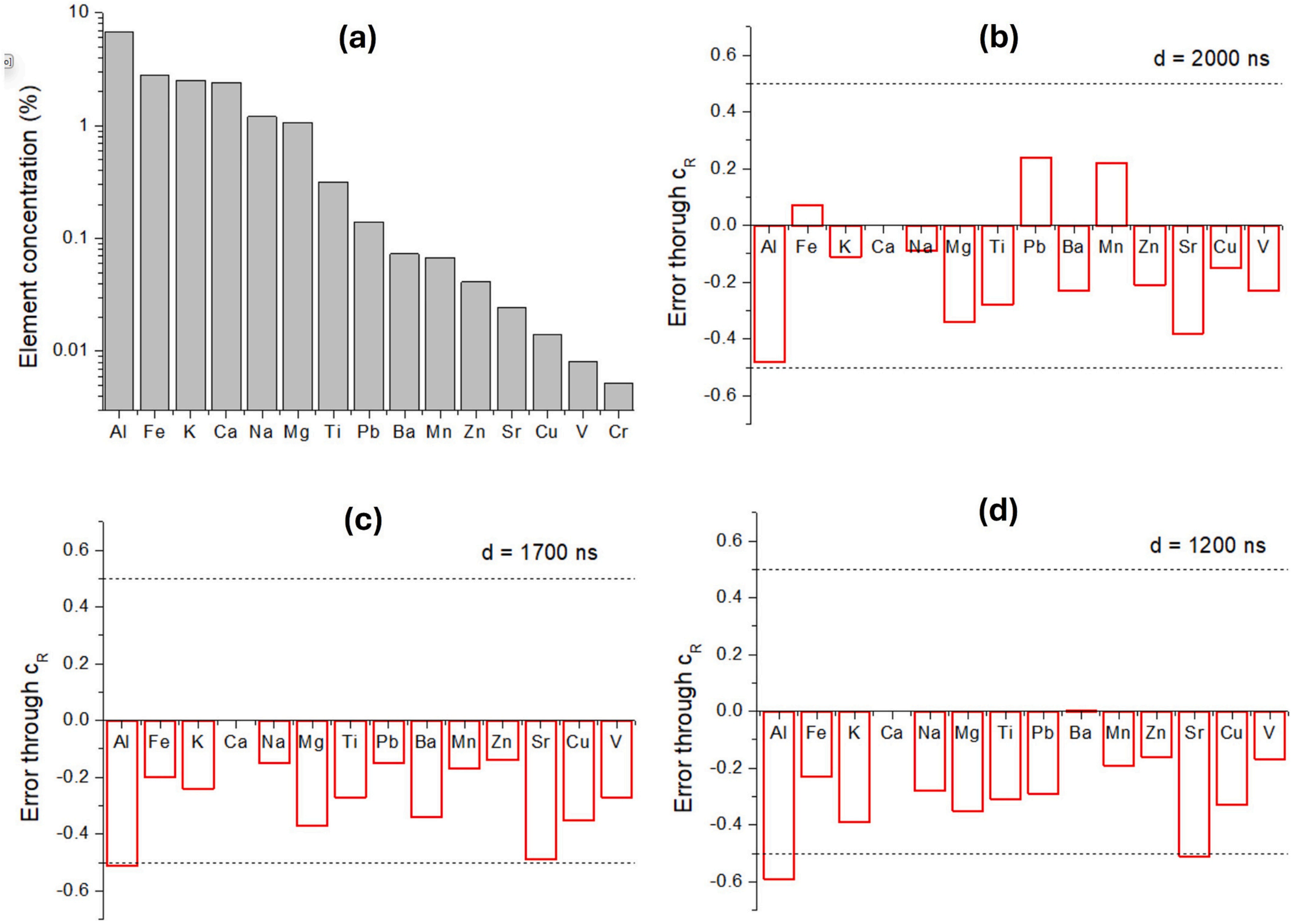

Fig. 11. Certified element concentrations in sample Soil3# (a), and the errors in determination of the element concentrations through the coefficients c_R on the pressed pellet, for the acquisition delays of: (b) 2000 ns, (c) 1700 ns and (d) 1200 ns.

Table 7
Summary of the indicator of plasma temperature RSi and of electron density found in calibration and validation measurements.

	Calibration		
Sample	**Acquisition delay (ns)**	**RSi**	**N_e (10^{17} cm^{-3})**
ST21#W	2000	0.073 ± 0.007	1.45 ± 0.05
Rock#W	2000	0.067 ± 0.021	1.6 ± 0.2
Soil1#W	2000	0.078 ± 0.026	1.7 ± 0.3
Soil2#A	2000	0.036 ± 0.018	1.3 ± 0.1
Soil3#W	2000	0.068 ± 0.23	1.7 ± 0.3
Soil4#W	2000	0.047 ± 0.15	1.2 ± 0.2
ASH#W	2000	0.056 ± 0.021	1.5 ± 0.2
COAL#W	2000	0.046 ± 0.015	1.3 ± 0.2
CaBa#W	2000	0.072 ± 0.018	1.3 ± 0.1
Validation			
Soil2#W	2000	0.061 ± 0.029	1.5 ± 0.2
Soil2#P	2000	0.027	1.2
Soil3#P	2000	0.040	1.2
	1700	0.056	2.2
	1200	0.081	2.8

applying Abelian inversion. However, even with spatially integrated acquisition, RSi is a good indicator of excitation conditions, and its value helps evaluating changes of the plasma parameters inside the data set.

3.4. Practical steps to use here reported calibration coefficients

The transferable calibration coefficients (TCCs) reported in Tables 5–6 are specific for the spectrometers used, where the spectral response S_R, reported in Table 3, is defined as:

$$S_R(\lambda) = \frac{I_M(\lambda)}{I_{HD}(\lambda)} \cdot F \tag{9}$$

Where I_M is the measured spectral intensity (in counts) at certain wavelength λ, at which the calibration Halogen-Deuterium (HD) source has defined or extrapolated irradiance I_{HD}, usually expressed in μW/cm^2/nm. The coefficient F is fixed, and in our case it was chosen to have the maximum value of 1000 among the considered analytical lines. Considering that we deal with calibration respect to the internal standard (one Ca line), the multiplication factor F does not affect the results.

To apply here extrapolated calibration coefficients (Tables 5–6) to another LIBS system, the specific spectral response $S_R^S(\lambda)$ should be first determined experimentally, where it is important to apply the same exposure time for both Halogen and Deuterium lamp or to scale properly the measured intensity I_M when passing from one source to another. Successively, the peak intensity I_{el} of each element's line, including that from Ca, should be corrected (I_{el}^C) before applying the calibration coefficient c_B or c_R, as:

$$I_{el}^C(\lambda) = \frac{S_R^S(\lambda)}{S_R(\lambda)} \bullet I_{el}(\lambda) \tag{9}$$

Further requirements for applying the TCCs here derived, regard:

- Collection of the whole plasma emission
- Long integration time (here of 30 μs)
- Apparent plasma temperature close to 7000 K
- Apparent electron density close to $1.5 \cdot 10^{17}$ cm^{-3}
- Initial knowledge or guess of the sample composition, to select the calibration coefficients according to the concentration range if they cannot be considered constant.
- Similar spectral resolution

In our experiment, by using a nanosecond pulse laser at 1064 nm with 30 mJ pulse energy focused on 0.3 mm diameter spot, the effective acquisition delay from the laser pulse was set to 2 μs. Note that due to detector's specific electronic delay, typically in order of 1 μs for compact spectrometers, to achieve the effective delay from the laser pulse it is necessary to pre-trigger properly the spectrometers and synchronize them with the laser pulse.

For here employed instrument, detection of the Cu I peak at 515 nm indicated that concentration of this element was in order of 0.1% or higher, so the calibration coefficients for Cu should be taken for this range. Some departure from the optimal plasma parameters was not extremely critical for semi-quantitative LIBS analysis, still allowing the concentration measurements inside the error of ±50% for most of the considered elements (see Fig. 11). It should be kept in mind that accurate LIBS analysis requires the use of matrix-matched standards. In case of need for rapid multielement analysis of samples with different or unknown matrix, the semiquantitative methods, even with the errors are higher than the typical 10–50% estimated in the presented work, still can be considered satisfactory for many application purposes.

Regarding the spectral resolution, here high for common wide spectral range detectors, the transfer of the calibration towards lower resolution systems is feasible through the binning [29]. For example, we checked the ratio of Mg and Ca lines used for the calibration: after binning two adjacent spectral points to simulate a twice lower resolution, the peak ratio Mg/Ca was reduced for about 18%. This change in the peak ratio affects the measuring accuracy by using the TCCs, but it still allows semi-quantitative estimation of Mg in sample.

4. Conclusions

LIBS measurements on particles over a substrate that enhances the plasma emission, like Si wafer or aluminium, minimizes the matrix effect and allows changing of the spectral line intensities and plasma parameters by varying a sample amount and distribution inside the laser spot. Another advantage of this sampling approach regards a very low sample consumption (< 1 mg) while the use of two substrates, like silica wafer and aluminium, makes possible to also estimate Al and Si contents in samples, respectively. For this measuring modality, the calibration coefficients were generated on known samples with dissimilar matrixes, both through the linear peak growth (coefficient c_B) respect to the selected Ca line and the peak ratio (c_R) for 14 elements. The first calibration approach produced the relative concentration measurements with accuracy better than ±30% for 13 elements while the error for Zn was of about 40%. Considering a large number of the measured elements, their abundancies from traces to major constituents, and simplicity of the method, here obtained results could be considered very promising for multi-element quantification by LIBS.

For some line pairs, the concentration measurements through the line ratio are very sensitive to changes of the plasma parameters and line's self-absorption compared to the previous method, as confirmed by the theoretical simulations. The accuracy in determination of the relative element concentration through the line ratio is particularly reduced for elements measured through resonant lines and/or which abundancies are at limits of here established calibration range. However, even with a moderate mismatching of the plasma parameters, here monitored through ratio of ionic to atomic Si lines and Stark broadening of H_α line, semiquantitative analysis within the error of ±50%, could be still performed except for Al, Cr and Na. Nonetheless these limitations, the method is applicable also on bulk samples (pressed pellets or solid fragments) and on trace samples where the LIBS probing is limited to a single or very few laser pulses.

Transition from relative to absolute element concentrations in sample by using here supplied calibration coefficients, could be achieved or through the initial knowledge of Ca concentration in sample, or through normalization of relative abundancies from all detected elements, including Ca, to the sum of 100% or else. In the latter case, it is important to consider the eventual presence of not measured elements, like oxygen, and attribute their weight (e.g. specific element's oxides) in the concentration closure.

Here retrieved transferable calibration coefficients (TCCs) could be evaluated on different LIBS instruments thanks to the method's simplicity, supplied spectral responses for each analytical line and corresponding instructions. The observed and explained behaviour of the calibration coefficients with changes of the plasma parameters and element concentrations, also provides a valuable input for selection of the analytical lines in LIBS, for building a model relative to multivariate calibration, and helps understanding the actual limits in the quantification accuracy.

Further research regards the measurements on a larger number of samples than here, the extension of the calibration coefficients to other elements and line transitions, as well as studies aimed to better understand and overcome limits in quantitative multielement analysis by LIBS.

CRediT authorship contribution statement

V. Lazic: Writing – original draft, Methodology, Investigation, Formal analysis, Data curation, Conceptualization. **M. Markovic:** Formal analysis. **B.D. Stankov:** Investigation, Formal analysis. **F. Andreoli:** Software. **C. Ulrich:** Writing – review & editing, Investigation. **M. Kuzmanovic:** Writing – review & editing, Methodology, Investigation, Conceptualization.

Declaration of competing interest

The authors have no conflicts of interest to declare.

Acknowledgements

A part of this research was performed inside Real-tIme on-site forenSic tracE qualificatioN (RISEN) project, funded by the European Commission, grant number 883116.

Appendix A. Supplementary data

Supplementary data to this article can be found online at https://doi.org/10.1016/j.sab.2026.107454.

Data availability

Data will be made available on request.

References

[1] D.W. Hahn, N. Omenetto, Laser-induced breakdown spectroscopy (LIBS), part II: review of instrumental and methodological approaches to material analysis and applications to different fields, Appl. Spectrosc. 66 (2012) 347–419, https://doi.org/10.1366/11-06574.

[2] D.A. Cremers, L.J. Radziemsky, Handbook of laser-induced breakdown spectroscopy, John Wiley&Sons Ltd., 2013, https://doi.org/10.1002/9781118567371.

[3] C. Alvarez-Llamas, A. Tercier, C. Ballouard, C. Fabre, S. Hermelin, J. Margueritat, L. Duponchel, C. Dujardin, V. Motto-Ros, Ultrafast μLIBS imaging for the multiscale mineralogical characterization of pegmatite rocks, J. Anal. At. Spectrom 39 (2024) 1077–1086, https://doi.org/10.1039/D3JA00438D.

[4] V. Lazic, M. Vadrucci, R. Fantoni, M. Chiari, A. Mazzinghi, A. Gorghinian, Applications of laser induced breakdown spectroscopy for cultural heritage: a comparison with XRF and PIXE techniques, Spectrochim. Acta B 149 (2018) 1–14, https://doi.org/10.1016/j.sab.2018.07.012.

[5] V.C. Costa, D.V. Babos, J.P. Castro, D.F. Andrade, R.R. Gamela, R.C. Machado, M. A. Sperança, A.S. Araújo, J.A. Garcia, E.R. Pereira-Filho, Calibration strategies applied to laser-induced breakdown spectroscopy: a critical review of advances and challenges, J. Braz. Chem. Soc. 31 (2020) 2439–2451, https://doi.org/10.21577/0103-5053.20200175.

[6] I.B. Gornushkin, J.M. Anzano, L.A. King, B.W. Smith, N. Omenetto, J. D. Winefordner, Curve of growth methodology applied to laser-induced plasma emission spectroscopy, Spectrochim. Acta Part B 54 (1999) 491–503, https://doi.org/10.1016/S0584-8547(99)00004-X.

[7] J.A. Aguilera, C. Aragón, Characterization of a laser-induced plasma by spatially resolved spectroscopy of neutral atom and ion emissions. Comparison of local and spatially integrated measurements, Spectrochim. Acta Part B 59 (2004) 1861–1876, https://doi.org/10.1016/j.sab.2004.08.003.

[8] C. Chaleard, P. Mauchien, N. Andre, J. Uebbing, J.L. Lacour, C. Geertsen, Correction of matrix effects in quantitative elemental analysis with laser-ablation optical-emission spectrometry, J. Anal. At. Spectrom 12 (1997) (1997) 183–188, https://doi.org/10.1039/A604456E.

[9] U. Panne, C. Haisch, M. Clara, R. Niessner, Analysis of glass and glass melts during the vitrification process of fly and bottom ashes by laser-induced plasma spectroscopy. Part I: normalization and plasma diagnostics, Spectrochim. Acta Part B 53 (1998) 1957–1968, https://doi.org/10.1016/S0584-8547(98)00239-0.

[10] V. Lazic, R. Fantoni, F. Colao, A. Santagata, A. Morone, V. Spizzichino, Quantitative laser induced breakdown spectroscopy analysis of ancient marbles and corrections for the variability of plasma parameters and of ablation rate, J. Anal. At. Spectrom 19 (2004) 429–436, https://doi.org/10.1039/B315606K.

[11] V. Lazic, A. Trujillo-Vazquez, H. Sobral, C. Márquez, A. Palucci, M. Ciaffi, M. Pistilli, Corrections for variable plasma parameters in laser induced breakdown spectroscopy: application on archeological samples, Spectrochim. Acta Part B 122 (2016) 103–113, https://doi.org/10.1016/j.sab.2016.06.003.

[12] N.B. Zorov, A.A. Gorbatenko, T.A. Labutin, A.M. Popov, A review of normalization techniques in analytical atomic spectrometry with laser sampling: from single to multivariate correction, Spectrochim. Acta Part B 65 (2010) 642–657, https://doi.org/10.1016/j.sab.2010.04.009.

[13] E. Tognoni, G. Cristoforetti, S. Legnaioli, V. Palleschi, Calibration-free laser-induced breakdown spectroscopy: state of the art, Spectrochim. Acta Part B 65 (2010) 1–14, https://doi.org/10.1016/j.sab.2009.11.006.

[14] S.V. Shabanov, I.B. Gornushkin, Geometrical effects in data collection and processing for calibration-free laser-induced breakdown spectroscopy, J. Quant. Spectrosc. Radiat. Transf. 204 (2018) 190–205, https://doi.org/10.1016/j.jqsrt.2017.09.018.

[15] J. Hermann, F. Pelascini, Calibration-free laser-induced breakdown spectroscopy: Toward industrialization, in: V.K. Singh (Ed.), Laser Induced Breakdown Spectroscopy (LIBS), Springer, Cham, 2025, https://doi.org/10.1007/978-3-031-90970-2_5.

[16] C. Gerhard, A. Taleb, F. Pelascini, J. Hermann, Quantification of surface contamination on optical glass via sensitivity-improved calibration-free laser-induced breakdown spectroscopy, App. Surf. Sci. 537 (2021) 147984, https://doi.org/10.1016/j.apsusc.2020.147984.

[17] N.B. Zorov, A.M. Popov, S.M. Zaytsev, T. Labutin, Qualitative and quantitative analysis of environmental samples by laser-induced breakdown spectrometry, Russ. Chem. Rev. 84 (2015) 1021–1050, https://doi.org/10.1070/RCR4538.

[18] R.S. Harmon, R.E. Russo, R.R. Hark, Applications of laser-induced breakdown spectroscopy for geochemical and environmental analysis: a comprehensive review, Spectrochim. Acta B 87 (2013) 11–26.

[19] R.C. Wiens, S. Maurice, J. Lasue, O. Forni, R.B. Anderson, S. Clegg, S. Bender, D. Blaney, B.L. Barraclough, A. Cousin, L. Deflores, D. Delapp, M.D. Dyar, C. Fabre, O. Gasnault, N. Lanza, J. Mazoyer, N. Melikechi, P.-Y. Meslin, H. Newsom, A. Ollila, R. Perez, R.L. Tokar, D. Vaniman, Pre-flight calibration and initial data processing for the ChemCam laser-induced breakdown spectroscopy instrument on the Mars science laboratory rover, Spectrochim. Acta Part B 82 (2013) 1–27.

[20] J.M. Anzano, M.A. Villoria, A. Ruız-Medina, R.J. Lasheras, Laser-induced breakdown spectroscopy for quantitative spectrochemical analysis of geological materials: effects of the matrix and simultaneous determination, Anal. Chim. Acta 575 (2006) 230–235.

[21] J. Frydenvang, K.M. Kinch, S. Husted, M.B. Madsen, An optimized calibration procedure for determining elemental ratios using laser-induced breakdown spectroscopy, Anal. Chem. 85 (2013) 1492–1500, https://doi.org/10.1021/ac3026652.

[22] J.W. Batista Braga, L.C. Trevizan, L.C. Nunes, I.A. Rufini, D. Santos, F.J. Krug, Comparison of univariate and multivariate calibration for the determination of micronutrients in pellets of plant materials by laser induced breakdown spectrometry, Spectrochim.Acta Part B 65 (2010) 66–74, https://doi.org/10.1016/j.sab.2009.11.007.

[23] A. Erler, D. Riebe, T. Beitz, H-G. Löhmannsröben, R. Gebbers, Soil nutrient detection for precision agriculture using handheld laser-induced breakdown spectroscopy (LIBS) and multivariate regression methods (PLSR, lasso and GPR), Sensors 20 (2020) 418. doi:https://doi.org/10.3390/s20020418.

[24] G. Guo, G. Niu, Q. Shi, Q. Lin, D. Tian, Y. Duan, Multi-element quantitative analysis of soils by laser induced breakdown spectroscopy (LIBS) coupled with univariate and multivariate regression methods, Anal. Methods 11 (2019) 3006–3013, https://doi.org/10.1039/C9AY00890J.

[25] C. Sun, Y. Tian, L. Gao, Y. Niu, T. Zhang, H. Li, Y. Zhang, Z. Yue, N. Delepine-Gilon, J. Yu, Machine learning allows calibration models to predict trace element concentration in soils with generalized LIBS spectra, Sci. Reports 9 (2019) 11363, https://doi.org/10.1038/s41598-019-47751-y.

[26] J. Guezenoc, L. Bassel, A.G. Budynek, B. Bousquet, Variables selection: a critical issue for quantitative laser-induced breakdown spectroscopy, Spectrochim. Acta Part B 134n (2017) 6–10, https://doi.org/10.1016/j.sab.2017.05.009.

[27] L.-N. Li, X.-F. Liu, W.-M. Xu, J.-Y. Wang, R. Shu, A laser-induced breakdown spectroscopy multi-component quantitative analytical method based on a deep convolutional neural network, Spectrochim. Acta B 169 (2020) 105850, https://doi.org/10.1016/j.sab.2020.105850.

[28] K.H. Lepore, M.D. Dyar, C.R. Ytsma, Effect of plasma temperature on major element prediction accuracy from laser-induced breakdown spectroscopy, Geophys. Res. Lett. 50 (2023), https://doi.org/10.1029/2023GL102919, 2023GL102919.

[29] K.H. Lepore, M.D. Dyar, C.R. Ytsma, Sharing calibration information among laser-induced breakdown spectroscopy instruments using spectral line binning and calibration transfer, Spectrochim. Acta Part B 211 (2024) 106839, https://doi.org/10.1016/j.sab.2023.106839.

[30] J.R. Laura, L.R. Gaddis, R.B. Anderson, I.P. Aneece, Introduction to the Python Hyperspectral Analysis Tool (PyHAT), in: Machine Learning for Planetary Science, Elsevier, 2022, https://doi.org/10.1016/B978-0-12-818721-0.00012-4.

[31] V. Lazic, A. De Ninno, Calibration approach for extremely variable laser induced plasmas and a strategy to reduce the matrix effect in general, Spectrochim. Acta B 137 (2017) 28–38, https://doi.org/10.1016/j.sab.2017.09.001.

[32] M. Vinić, E. Aruffo, F. Andreoli, M. Ivković, V. Lazic, Quantification of heavy metals in oils with µL volume by laser induced breakdown spectroscopy and minimazing of the matrix effect, Spectrochim. Acta Part B 164 (2020) 105765, https://doi.org/10.1016/j.sab.2020.105765.

[33] V. Lazic, F. Andreoli, S. Almaviva, M. Pistilli, I. Menicucci, C. Ulrich, F. Schnürer, R. Chirico, A novel LIBS sensor for sample examinations on a crime scene, Sensors 24 (2024) 1469, https://doi.org/10.3390/s24051469.

[34] J.J. Olivero, R.L. Longbothum, J. Quant. Spectrosc. Radiat. Transf. 17 (1977) 233, https://doi.org/10.1016/0022-4073(77)90161-3.

[35] M.A. Gigosos, M.Á. González, V. Cardeñoso, Computer simulated Balmer-alpha, –beta and - gamma Stark line profiles for non-equilibrium plasmas diagnostics, Spectrochim. Acta Part B 58 (2003) 1489–1504, https://doi.org/10.1016/S0584-8547(03)00097-1.

[36] V. Lazic, R. Fantoni, S. Falzone, C. Gioia, E.M. Loreti, Stratigraphic characterization of ancient Roman frescos by laser induced breakdown spectroscopy and importance of a proper choice of the normalizing lines, Spectrochim. Acta Part B 168 (2020) 105853, https://doi.org/10.1016/j.sab.2020.105853.

[37] T.A. Labutin, S.M. Zaytsev, A.M. Popov, I.V. Seliverstova, S.E. Bozhenko, N. B. Zorov, Comparison of the thermodynamic and correlation criteria for internal standard selection in laser-induced breakdown spectrometry, Spectrochim. Acta Part B 87 (2013) 57–64, https://doi.org/10.1016/j.sab.2013.05.021.